ELSEVIER

Contents lists available at ScienceDirect

Chemical Engineering Journal

journal homepage: www.elsevier.com/locate/cej





Combined silicon refining for boron removal and Si-Kerf recycling using K₂O-CaO-SiO₂ slags

Mengyi Zhu a,*, Guixuan Wu b,*, Kai Tang c, Michael Müller b, Jafar Safarian a

- a Department of Materials Science and Engineering, Norwegian University of Science and Technology (NTNU), Trondheim, Norway
- b Institute of Energy and Climate Research, Structure and Function of Materials (IEK-2), Forschungszentrum Jülich GmbH, Germany
- ^c SINTEF Industry, N-7465 Trondheim, Norway

ARTICLE INFO

Keywords:
Silicon
Impurity
Slag refining
Slag structure
Molecular dynamics simulation
Thermodynamics

ABSTRACT

It is crucial for the photovoltaic (PV) industry to establish a circular materials flow for more sustainable solar silicon production. In the present work, a series of K_2O -SiO $_2$ and K_2O -CaO-SiO $_2$ slags were examined for the combination of silicon purification and Si-kerf waste recycling. The study revealed that the predominant mass transfer mechanism and the variation in slag composition during refining are due to the silicothermic reduction of K_2O . The boron removal degree reached levels above 80% in most of tests, with boron gasification as potassium metaborate confirmed as an important mechanism for boron removal, especially in slags with high K_2O content. In the case of ternary slags, the results indicated that an increase in CaO enhances boron partitioning in slag phase and a high K_2O content also led to boron accumulation in the slag phase due to rapid reaction kinetics in the early stage of refining. The distinct behaviours of calcium and postassium ions in the slag phase were revealed by molecular dynamics simulations. It was found that potassium ions preferentially modify bridging oxygen, while calcium ions contribute more to depolymerizing the tectosilicate network and generating more non-bridging oxygens, which may further aid in the boron stabilization in slag phase. The oxidation layer of Si-kerf was removed successfully and enabled the coalescence of the silicon nanoparticles into the Si melt. Additionally, the presence of SiC clusters in the slag phase was also observed, indicating effective removal of SiC and the feasibility of Si-kerf waste recycling.

1. Introduction

Solar energy is critical in the transition to carbon neutrality and minimizing the effects of climate change. In recent years, the solar photovoltaic (PV) market has expanded exponentially in response to the rising global demand for renewable energy. According to the International Energy Agency [1], solar PV power production increased by a record 179 TWh in 2021, ushering in a new era of 1000 TWh solar energy production worldwide. Crystalline silicon is by far the most dominant PV material used in solar cells. The solar-grade silicon (SoG-Si, 6 N purity 99.9999 %) is produced through refining process to remove impurities on the basis of less pure metallurgical-grade silicon (MG-Si, 2 N purity 99 %).

Nowadays, the SoG-Si is predominantly produced using the Siemens process and the fluidized bed reactor (FBR) process. The former process reduces trichlorosilane to ultra-high purity silicon (10 N to 11 N). Even though it has been in operation for decades, this process is considered

energy-intensive since its sluggish decomposition kinetics necessitates a long heating time of the rod reactor at around $1100\,^{\circ}$ C. The FBR process is a more recent development that is more energy efficient. However, the reduction in energy consumption is still limited and it requires specialized equipment, which complicates the process and raises the production cost. Additionally, both methods may also bring negative impacts on the environment, as they produce a large number of pollutants, such as greenhouse gas emissions and other hazardous wastes. Thus, there is still substantial room for the SoG-Si market to become more sustainable.

Moreover, there is another urgent concern for the PV industry, which concerns the recycling of the silicon kerf waste from the wafering process. As the high-value SoG-Si ingot must be sliced into wafers by multiwire sawing, a considerable amount of high-purity Si is lost, accounting for 40 % to 50 % of the total SoG-Si used [2]. The waste slurry usually consists of abrasive SiC particles, polyethylene glycol or mineral oil coolant, and shreds of metallic fragments. Due to its chemical resistance and physical attributes similar to Si, separating the SiC from Si kerf

E-mail addresses: mengyi.zhu@ntnu.no (M. Zhu), g.wu@fz-juelich.de (G. Wu).

^{*} Corresponding authors.

remains a great challenge. Recycling kerf can not only alleviate the shortage of SoG-Si material but also provide the PV industry with considerable environmental and economic benefits.

As an emerging and transformational technology for alternate SoG-Si production, the metallurgical refining route provides a promising solution for the aforementioned issues to form a circular Si value chain [3]. First, compared to the conventional methods, the metallurgical process has significantly lower energy consumption and carbon footprint. For instance, in the Elkem Solar process, it combines slag refining [4] for B removal and acid leaching [5,6] for P removal at low operation temperature. Thus, it is estimated to have a total energy consumption be between 30 and 60 kWh/kg Si, which is significantly less than both the Siemens process (~170 kWh/kg Si) and the FBR-Si process (75-95 kWh/ kg Si). Furthermore, the capacity of the metallurgical refining methods to couple with cutting kerf recycling is also a significant advantage. The slag refining process, which is a key part of the Elkem Solar process, is particularly effective at separating SiC from the cutting kerf due to the superior wettability between SiC and molten slag, enabling the recovery of a high percentage of high-purity silicon. Thus, the unique advantages have helped the development of metallurgical routes for SoG-Si production gain significant attention from academics and industry in recent years due to the distinct benefits.

There has been extensive research on slag refining, with studies exploring a wide range of slag systems from binary to quaternary, such as CaO-SiO₂ [7], CaO-SiO₂-CaF₂ [8], CaO-MgO-SiO₂ [9], and CaO-MgO-Al₂O₃-SiO₂ [4,10]. Moreover, slags that facilitate the conversion of boron impurities into gaseous products have also sparked considerable interest. The advantage lies in its independence from chemical equilibrium constraints, thereby facilitating profound boron removal. Safarian et al. [11,12] reported that B can be rapidly removed using the Na₂O-SiO₂ slag system through the formation of volatile compound sodium metaborate (Na₂B₂O₄). Fang et al. [13] performed multiple operation of Na₂O-SiO₂ slag refining to decreased B content below 0.3 ppmw. Moreover, the addition of Li₂O [14,15] and K₂CO₃ [16,17] also reveals high efficiency for boron removal [18–20]. However, it is still uncertain whether K2O-containing slags stabilize boron within the slag phase or facilitate its conversion into a gaseous state for removal, especially during the slag refining of silicon with extremely low B content at the ppmw level.

In addition, since the presence of the thin $\mathrm{Si}_x\mathrm{O}_y$ oxide layer on the Sikerf powder surface complicates the direct recycling of kerf, slag refining has emerged as a promising solution to overcome the issues. In recent years, it has been demonstrated the presence of $\mathrm{Na}_2\mathrm{O}$ in the slag system also facilitates the cutting kerf recycling [18] and aids in the SiC separation [19]. Nonetheless, despite potassium element is known to have a stronger erosive effect on SiC than sodium [20], the implications of $\mathrm{K}_2\mathrm{O}$ -based slag system on kerf recycling remains undiscovered.

Therefore, it is critical to investigate the K_2O -containing slag refining system combined with kerf recycling. Hence, in this work, a series of binary and ternary K_2O -CaO-SiO $_2$ slag systems were investigated, aiming to reveal the effects and mechanisms of boron removal. Concurrently, the recycling of kerf waste during slag refining was also studied, seeking to attain the dual benefits of silicon purification and kerf recovery within a singular process to form a circular materials flow.

2. Experimental

2.1. Raw materials

Commercial-grade silicon fines (HQ-Silgrain®) were utilized as the initial silicon raw materials for slag refining. Additionally, silicon cutting kerf powder was also introduced to evaluate its recycling performance through slag refining. For the purpose of dual benefits refining conducted in this work, the two different silicon sources were employed together with a ratio of 3:1 served as the metal phase in slag refining, resulting a B content of 25.8 ppmw in total. The quantified impurity

concentrations of the silicon sources used are outlined in Table 1.

The master slags were prepared through a melt-casting procedure by smelting with the reagent grade $\rm K_2CO_3$ (99.9 %, Sigma-Aldrich), CaO (99.9 %, Sigma-Aldrich), and ultra-high purity $\rm SiO_2$ fines (The Quartz Corp). The raw materials were homogenously mixed in accordance with the target slag composition and charged into a dense graphite crucible for heating. Once completely melted in an induction furnace, the molten slag was cast into a water-cooled copper mold. The cast synthetic binary and ternary slags were then crushed and milled to achieve homogenization. The composition of obtained slag is listed in Table 2. It should be noted that in the studied ternary slag system, the initial $\rm SiO_2$ molar fraction before the refining process begins is fixed at approximately 0.45 with varying $\rm K_2O/(K_2O+CaO)$ ratio.

2.2. Methods

2.2.1. Experimental

The slag refining experiments were performed in a medium frequency induction furnace under Ar gas (99.9999 %) atmosphere. The obtained synthetic master slags were first dried overnight in a drying oven and then placed into the lower part of a SiC crucible at a slope angle to enhance the contact surface area. The kerf waste was placed above slag layer and covered by the Silgrain fines. The slag/silicon/kerf mass ratio was fixed as 8:3:1 (slag/silicon = 2). In the KCS-1 trial, a larger SiC crucible (50 mm inner diameter 50 mm, 120 mm height) was employed. The experiment utilized 40 g of slag along with 5 g of kerf waste and 15 g of Silgrain Si fine particles. For the subsequent experiments, a smaller SiC crucible (32 mm inner diameter, 54 mm height) was used, and the charged weights were 12 g of slag, 1.5 g of kerf waste, and 4.5 g of Silgrain Si fine particles.

The SiC crucible was further put into a bigger graphite crucible (inner diameter: 70 mm, height: 150 mm). Before heating, the furnace chamber was vacuumed and refilled by Ar gas for three times. During the experiments, the chamber pressure was controlled at around $1030{-}1060$ mbar manually with continuous Ar gas flow. The temperature was measured by a Type-C thermocouple and kept at $1600\,^{\circ}\text{C}$ for two hours. After refining experiment, samples were cooled down to room temperature inside the furnace and then collected for further metallographic and chemical analysis.

2.2.2. Computational simulation

The significant loss of K during the slag refining process led to substantial changes in slag structure and properties. Thus, force field Molecular Dynamics (MD) simulations of the $K_2O\text{-}CaO\text{-}SiO_2$ system were conducted to gain further insights into this phenomenon using the Large-scale Atomic/Molecular Massively Parallel Simulator (LAMMPS) package. In this study, four distinct compositional points are considered in each slag simulation, capturing slag composition before and after refining, as well as during nominal reductions of K_2O by one-third and two-thirds. The detailed slag composition used for simulation and the number of input atoms are listed in Table S1.

Interatomic interactions between K_2O -CaO-SiO₂ were described using Teter's Buckingham potential parameters [21] and listed in Table 3. The potential energy described by the long-range Columbic interaction term and the short-range interaction term. As can be seen in Equation (1), where r_{ij} denotes the distance between atom i and j. The columbic interaction is characterized by the first term, with z_i represents

Impurity concentration (ppmw) of studied Si-source for the slag refining treatment.

Si-source	Ca	В	P	Al	Fe	K
Silgrain	125.4	34.45	27.15	858.5	382.4	3.0
Kerf	22.9	<0.05	<0.5	2.5	<2.0	3.0
Mixture	99.8	25.8	20.4	644.5	286.8	3.0

Table 2Chemical composition of obtained slags for slag refining.

Slags	Initial composition (mol%)			Initia	Initial composition (wt%)		
	SiO_2	K ₂ O	CaO	SiO_2	K ₂ O	CaO	
KS-0	45.0	55.0	-	34.3	65.7	_	
KS-1	54.9	45	0.1	43.7	56.2	0.03	
KS-2	72.1	27.8	0.1	62.2	37.7	0.04	
KCS-1	44.7	43.9	11.4	35.9	55.5	8.6	
KCS-2	46.4	32.6	21	39.6	43.7	16.7	
KCS-3	47.9	23.4	28.7	43.0	33.0	24.0	
KCS-4	46.2	12.1	41.7	44.3	18.2	37.4	

Table 3 Atomic charges and interatomic parameters of the adopted potential.

Pair (i-j)	$z_i(e)$	A (ev)	$ ho(ext{Å})$	C (ev $Å^6$)
0–0	-1.2	2029.2204	0.343645	192.58
Si-O	2.4	13702.905	0.193817	54.681
Ca-O	1.2	7747.1834	0.252623	93.109
K-O	0.6	20526.972	0.233708	51.489

the effective charge of atom i, e and ε_0 stands for electric charge and the permittivity of vacuum. The parameters A_{ij} , ρ_{ij} , and C_{ij} are empirical parameters for specific atoms pair.

$$U_{ij}(r) = \frac{z_i z_j e^2}{4\pi \varepsilon_0 r_{ij}} + A_{ij} e^{-r_{ij}/\rho_{ij}} - \frac{C_{ij}}{r_{ij}^6}$$
(1)

The cut-off distance for interactions was set at 11 Å to ensure computational precision. Coulombic interactions were resolved using the Ewald summation method. The Verlet leapfrog algorithm was employed for the integration of motion equations, with a fixed timestep of 1 fs. For each simulation set, around 7000 atoms were randomly generated and distributed within a cubic box to construct a disordered initial configuration under periodic boundary condition. The system was then equilibrated at temperature of 3500 K and under an isothermalisobaric (NPT) ensemble for 500 picoseconds (ps) to reach thermodynamic equilibrium. Subsequently, the system was cooled down to 1873 K at a rate of 1 K/ps under the NPT ensemble, followed by a further 500 ps of relaxation in both the NPT and canonical (NVT) ensembles to guarantee system stability. Finally, a production run spanning 1.5 ns (ns) under the NVT ensemble was conducted to acquire reliable average properties.

2.3. Chemical analysis

After slag refining, the crucible was sectioned along its vertical axis into two halves, one was then prepared into metallographic samples for detailed examination. Microstructural characterization of the slag/metal interface was carried out using a Scanning Electron Microscope (SEM) accompanied by Energy Dispersive Spectroscopy (EDS) analysis. The rest slag and metal samples extracted from the other half were subjected to digestion using a mixture of HNO3 and HF solution, except the heavily evaporated KS-0 sample. Subsequent chemical analysis was performed using an Agilent 8800 Inductively Coupled Plasma Mass Spectrometry (ICP-MS) system, operating in Triple Quadropole (ICP-QQQ) configuration with an SPS 4 Autosampler. Quantification was carried out based on standards from Inorganic Ventures as internal controls.

3. Results

3.1. Slag compositions and mass changes

During the slag refining experiments, significant evaporation from crucible was observed in all trials, especially in those involving high K_2O

Table 4 Measured masses before and after refining experiments involving binary K_2O -SiO₂ (KCS) slag and ternary K_2O -CaO-SiO₂ (KCS) slags.

Exp.	Charged materials (g)	Initial masswith crucible (g)	Final masswith crucible (g)	Total mass loss (g)	Pct mass loss from melts (%)
KS-1	24.0	92.1	87.6	4.5	18.6
KS-2	24.0	93.5	91.2	2.3	9.7
KCS-1	80.0	982.5	965.5	16.5	20.6
KCS-2	24.0	93.1	89.0	4.1	17.2
KCS-3	24.0	91.8	88.5	3.3	13.7
KCS-4	24.0	93.8	91.6	2.1	8.8

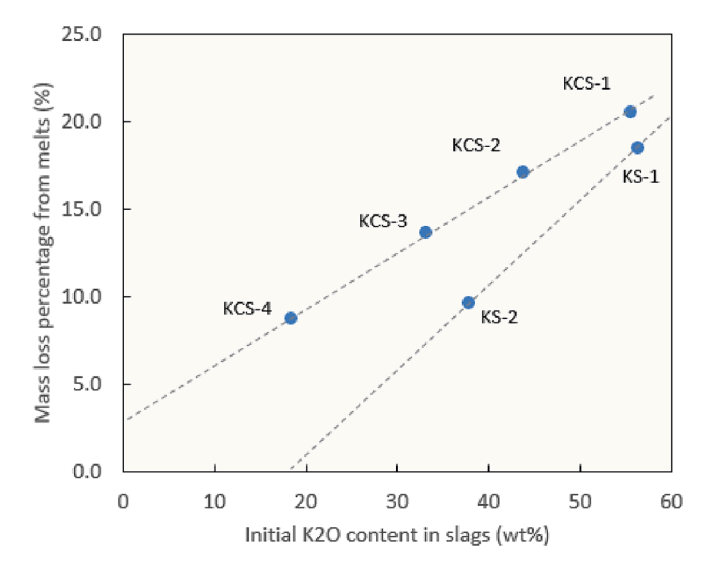


Fig. 1. Relationship between the initial K₂O content in slags and the final mass loss after experiments.

content slags. Furthermore, autoignition effects were also observed on the furnace wall when the furnace chamber was exposed to the ambient atmosphere. These observations indicate the presence of the evaporated and condensed alkali species. Hence, to quantify the mass loss level, the mass change of the refining system before and after experiments was measured and listed as Table 4.

Taking into account the percentage of mass loss to the whole slag and metal system, Fig. 1 is plotted. It is evident that the mass loss linearly related on the initial K_2O content in the slags. This implies that K_2O evaporation is likely the primary cause of the mass loss. Interestingly, it can be seen that, given a fixed initial K_2O content, the ternary slag refining systems exhibited a larger trend toward mass loss. This could possibly be attributed to the additional CaO content facilitates the kinetic conditions and slag chemistry for more volatile species formation.

Because of the massive mass loss, the slag and metal compositions changed significantly after experiments. Considering of the binary K_2O -SiO₂ slags, it is seen that the final slag compositions of KS-1 and KS-2 are almost the same with around 14–16 mol%. Another trend that can be seen is that with higher starting K_2O content in the slag, the final slag presents higher K_2O and SiO_2 content. For instance, the KCS-4 slag contains 12.1 mol% K_2O at first, while nearly all the K_2O was depleted in the final slag. But for KCS-1, the K_2O content decreases from the initial 43.9 mol% to the final 8.98 mol%, while the SiO_2 content dramatically increases from 44.7 mol% to 80.2 mol%.

3.2. Slag composition variation

The compositions of the final slags after slag refining are presented in Table 5. The initial and final changes in slag compositions in this work are shown in the K_2O -CaO-SiO $_2$ ternary system as Fig. 2. It can be seen

Table 5Chemical composition of final slags after refining.

Slags	Final composition (mol%)			Final	Final composition (wt%)		
	SiO_2	K ₂ O	CaO	SiO_2	K_2O	CaO	
KS-0	-	-	-	_	-	_	
KS-1	83.4	16.5	0.1	76.1	23.7	0.1	
KS-2	85.3	14.6	0.07	78.6	21.2	0.06	
KCS-1	80.2	9.0	10.9	76.7	13.5	9.7	
KCS-2	71.1	3.9	25.0	70.6	6.1	23.2	
KCS-3	65.6	1.9	32.5	66.3	3.0	30.6	
KCS-4	54.2	0.01	45.8	55.9	0.01	44.0	

that the changes in slag composition are directly proportional to the $\rm K_2O$ content. Furthermore, there is a deviation from the theoretical scenario in which only $\rm K_2O$ volatilizes, while the other components in the slag remain constant. This also indicates the presence of more complex mass transport in slag refining, which will be discussed in the following section. It should be noted that separation of the KS-0 slag and silicon phases was difficult due to the intense volatilization of slag KS-0. Hence, the composition of this experiment was not included, and it will also not be involved in subsequent discussions related to refining performance.

3.3. Refined silicon composition

The chemical composition of refined silicon was analyzed and the results are shown in Table 6. It is seen that the B content reduced significantly within the range 4–7 ppmw. Additionally, nearly all the Al was removed, and the Fe content partially removed. It was also found that the Ca concentration in the Si alloy increases with increasing CaO content in the slags from 208 ppmw to 4779 ppmw.

Table 6
Measured chemical composition of silicon phase after slag treatment (ppmw).

	Ca	В	K	Al	Fe	Ti
KS-1	9.6	5.2	780.6	1.8	212.1	13.0
KS-2	38.2	5.4	20.8	9.5	215	12.6
KCS-1	208.0	4.5	225.9	2.2	330.6	15.7
KCS-2	878.2	7.3	525.5	4.6	482.5	29.5
KCS-3	1216.0	5.4	n/a	9.2	304.9	18.4
KCS-4	4779.1	5.2	n/a	11.1	402.2	23.8

3.4. Melt geometry and phases contacts

Fig. 3 presents the image of cut crucible with slag and Si phase. It can be seen that from the KS-0 sample that a notable amount of residual dimple-shaped slag and Si metal particles were found adhering to the crucible wall. This phenomenon suggests intense slag volatilization that occurred in the KS-0 experiment due to the high initial K₂O content. Moreover, the direct contact between the slag phase and kerf powder resulted in a rapid increase in the viscosity of their mixture. This increased viscosity facilitated slag foaming effect and consequently led to the formation of a non-aggregated slag phase. However, effective separation between the slag and Si phase was observed from the other refining tests. Notably, the formation of a substantial single Si metal phase highlighted Si-kerf waste also underwent good melting. It is evident that its oxide layer was successfully removed during the process, which enabled the coalescence of the Si nanoparticles into the unified Si melt formed by the charged Si fine particles.

It was also observed that all Si phase settled at the bottom, and the slags did not flow on the top due to their lower density. Moreover, the Si melt did not directly contact the SiC crucible wall. Instead, a downward

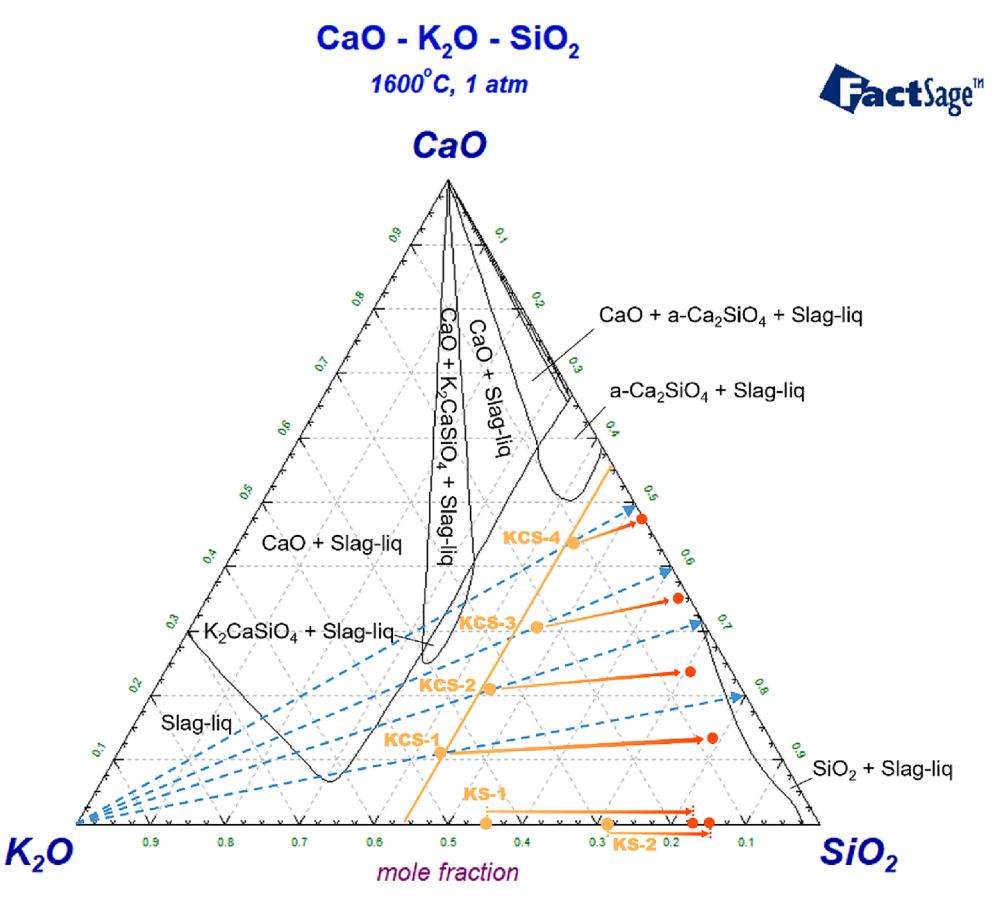


Fig. 2. Compositional change of the studied K_2O -CaO-SiO₂ slags compared with theoretical K_2O evaporation path (blue dash line), isothermal section at 1600 °C was calculated by FactSage thermodynamic software, version 8.1 [22]. (For interpretation of the references to colour in this figure legend, the reader is referred to the web version of this article.)

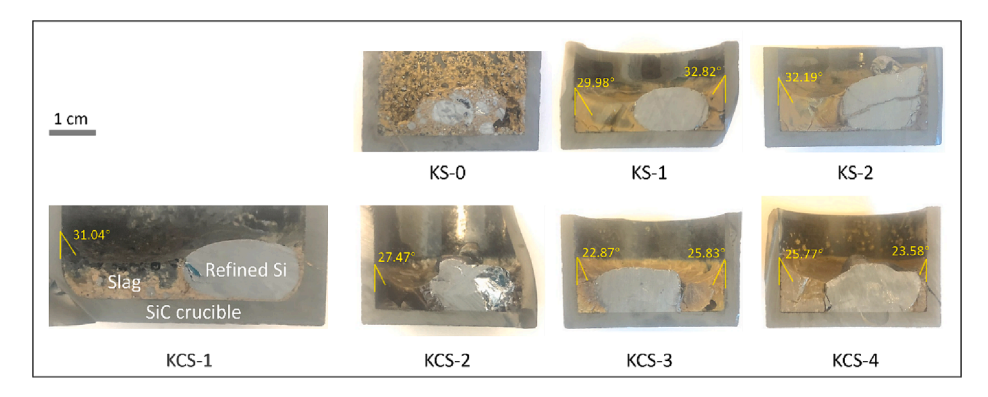


Fig. 3. Images of cross-sectional views of cut slag refining samples.

curving contact angle was formed between the slags and the SiC crucible wall, suggesting good wettability between the slags and SiC. This observation aslo suggests the preferential segregation of SiC particles into the slag phase.

To further investigate the wetting behaviour of slag with SiC, contact angles under Ar atmosphere between the slag and the SiC crucible were measured as a rough estimation. All contact angles between the slag and the silicon carbide were around 25-30°, considerably smaller than the measured contact angle for between the SiC/Si system ($\theta_{\alpha\text{-SiC/Si}}=38^\circ$ and $\theta_{\beta\text{-SiC/Si}}=41.5^\circ$)[23].

3.5. Microstructural analysis of slag/Si interface

To investigate the separation of SiC from the kerf powder, SEM was employed to examine the microstructure of the slag/Si interface in all samples. As illustrated in Fig. 4(a), the interface is populated by many hexagonal particles forming clustered regions, notably all situated on the slag side. These particles were further confirmed to be SiC through the EDS analysis, with the elemental mapping results presented in Fig. 4 (b). Furthermore, an observable trend is that as the particle size increases, their distance from the interface also expands correspondingly. This pattern implies that larger SiC particles may be more readily segregated from the interface.

4. Discussions

4.1. Mass transport between phases

During the refining test, significant mass loss was observed, indicating strong evaporation of volatile compounds occurred. As depicted in Fig. 1, the distinct relationship between the initial K_2O content in slags and the final mass loss has revealed that the K_2O related evaporation is the predominant contributor. However, there are different mechanisms attributing to the K loss, including the direct evaporation from slag phase, and silicothermic reduction-induced evaporation of metallic K from the metal phase.

4.1.1. Mechanism I – Direct evaporation from slag phase

Considering the evaporation from the slag phase, the following reaction must be taken into account:

$$(K_2O) = K_2O(g) \tag{2}$$

In addition, according to the observed autoignition effect on the furnace wall, the decomposition of K_2O may also occur that resulting in the release of gaseous potassium and oxygen:

$$(K_2O) = 2K(g) + \frac{1}{2}O_2(g)$$
 (3)

The gaseous potassium was then condensed as dusts, which was actively oxidized when exposed in the ambient atmosphere. Another

route led to mass loss may dedicated to the reaction between $K_2\mbox{O}$ and the SiC crucible,

$$(K_2O) + SiC = 2K(g) + CO(g) + SiO(g)$$
 (4)

Since the kerf layer with the dispersion of fine SiC particles were placed closely to the slag, such reaction may also take place along their interface that contributes to the total mass loss. In addition, chemical reaction (4) may proceed at the slag/crucible interface. From kinetics point of view chemical reaction (4) is possible in the system, while reaction (3) may have kinetics barrier.

4.1.2. Mechanism II – Indirect evaporation from Si phase

The depletion of K_2O in the slag could also result from the silicothermic reduction. The route for mass transfer is described as follows:

$$\frac{1}{2}Si + (K_2O) = 2[K] + \frac{1}{2}(SiO_2)$$
 (5)

The potassium reduced via silicothermic reduction is transferred to the Si/gas interface and then rapidly evaporates due to its high vapor pressure even though it is the dilute solute in Si melt:

$$[K] = K(g) \tag{6}$$

4.1.3. Quantitatively evaluation of the two mechanisms

It is imperative to quantitatively evaluate the impacts of both mechanisms. The distinguishing feature of Mechanism I is that the slag composition is solely influenced by the depletion of K_2O . Consequently, as shown in the ternary phase diagram of Fig. 2, the variation in slag composition moves along the dashed line originated from the K_2O corner, maintaining a consistent CaO/SiO_2 ratio. In contrast, Mechanism II results in an increased incorporation of SiO_2 mass into the slag phase, which induces a compositional shift favouring the SiO_2 side.[23] Thus, based on the measured SiO_2 content variation, the impact of the two mechanisms can be evaluated.

According to the mass loss data listed in Table 4, the final slag composition for each mechanism can be determined through mass balance calculations. The calculation results are displayed in Table 7. It can be observed that under the assumption of only Mechanism I took place, the final SiO_2 content in the slag is considerably lower than the measured value. Conversely, when only Mechanism II is considered, a higher SiO_2 content is yielded. Thus, it can be concluded that both mechanisms coexist during the experiments. Moreover, by comparing the measured values with the calculated ones from both mechanisms, the contribution of each mechanism to the mass loss can be further determined. The results are depicted in Fig. 5.

As observed in Fig. 5, within the binary $K_2O\text{-}SiO_2$ slag refining system, Mechanism I, which involves direct evaporation from the slag, plays a dominant role. However, it is also seen that although KS-1 slag possesses a higher K_2O content, the contribution from Mechanism I is less than that in the KS-2 slag, which has a lower K_2O content. This trend

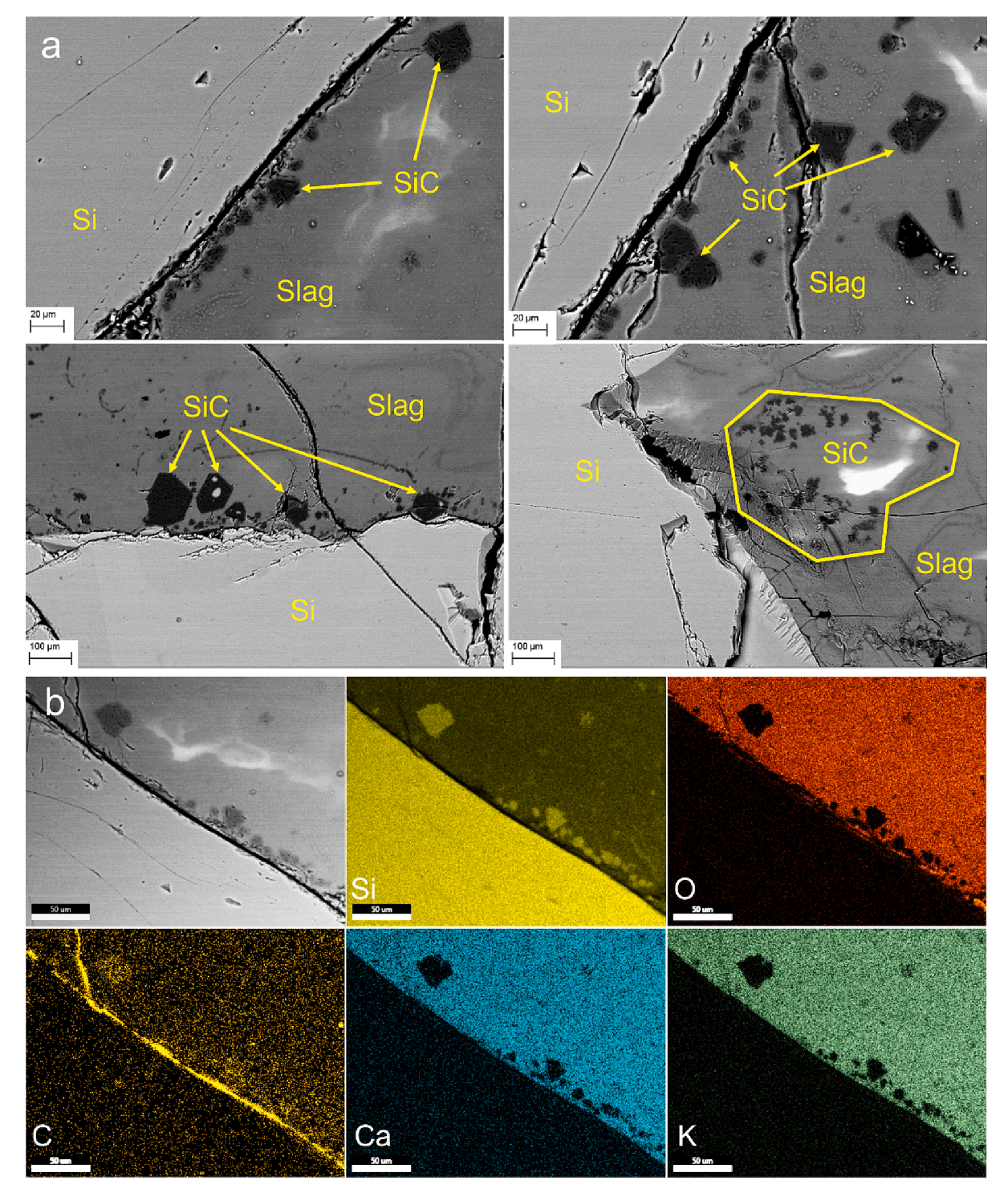


Fig. 4. (a) Backscattered electron image of the slag/Si interface, and (b) EDS elemental mapping at slag/Si interface of sample KCS-A.

 $\label{eq:Table 7} \textbf{Mass balance results for quantitatively evaluation of K_2O loss mechanisms.}$

Slag	Measured SiO ₂ in		Calculated SiO ₂ in w	t%	(Calculated final mass		
		t%						
	Before	After	Only Mechanism I	Only Mechanism II	Combined mechanisms	Final slag phase mass (g)	Final Si phase mass (g)	Slag/Si mass ratio
KS-1	43.73	76.09	69.60	83.49	76.44	8.34	5.63	1.48
KS-2	62.22	78.64	77.25	82.94	78.68	9.89	5.90	1.68
KCS-1	35.94	76.70	61.18	78.32	76.87	23.72	17.32	1.37
KCS-2	39.61	70.60	60.36	73.58	70.80	9.11	5.43	1.68
KCS-3	42.99	66.27	59.22	69.05	66.40	9.62	5.58	1.72
KCS-4	44.35	55.85	53.85	59.78	55.90	10.16	5.87	1.73

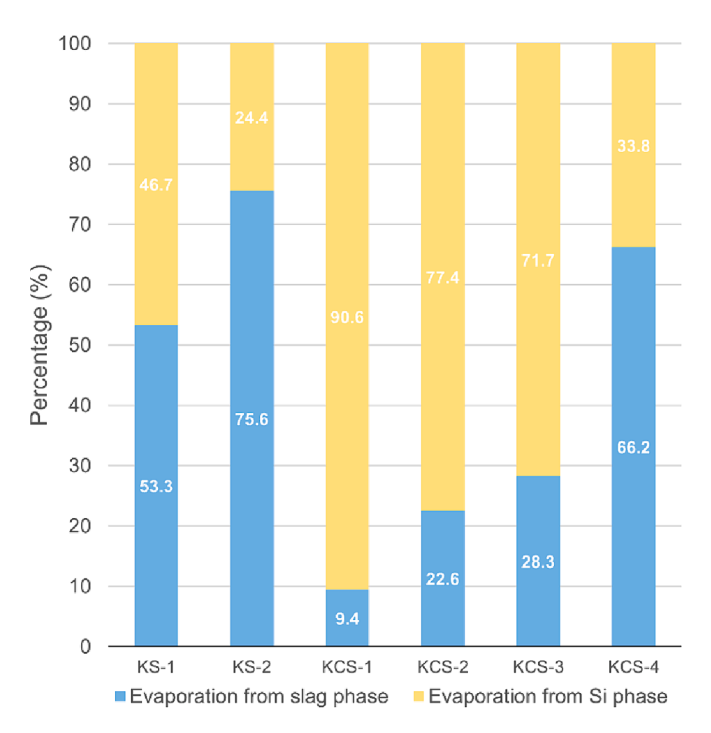


Fig. 5. Calculated contribution percentage of the two mechanisms for the $K_2\mathrm{O}$ loss.

might indicate that there was a significant portion of K_2O volatilized from the binary slagsduring the heating process, prior to the melting of Si phase. Subsequently, upon the formation of the Si melt, further mass loss is predominantly attributable to Mechanism II. Thus, given the higher initial K_2O concentration in KS-1, the driving force for Mechanism II is more pronounced, and accounting higher K_2O loss, 46.7 %, compared to only 24.4 % in KS-2.

The contribution from Mechanism II becomes even more pronounced in ternary systems, as demonstrated by the results of KCS-1, KCS-2, and KCS-3, where it plays a predominant role. As the CaO content increases, the driving force for Mechanism II decreases as the K_2O content drops. Consequently, the overall mass loss percentage of the system also decreases, as can be seen from Table 4, but the proportion of Mechanism I gradually rises accordingly.

4.2. Effect of K₂O evaporation on slag properties variation

4.2.1. Slag structure and viscosity

As the content of K₂O diminishes throughout the refining process, the slag structure and physicochemical properties of the slag correspondingly change. Fig. 6(a) illustrates the continual polymerization of the Si network due to K₂O evaporation from the binary slag. The planar slag network configurations are visualized from the snapshots of the simulated slags, using slabs with a thickness of 6 Å. It can be seen that in the initial state, SiO2 forms highly depolymerized structures, such as short chains. Then, these short chains progressively aggregate into ring structures and more complex network structures with the increase in SiO₂ content. This observed slag structrual polymerization process is in good agreement with the percolation theory [24] as a reversed process. As can be observed, when the K₂O concentration is at 25 %, a network modifier channel filled with a high concentration of K ions is clearly visible. Subsequently, with the continuous increase of SiO2, the connectivity between the channels diminishes until disappears. In the case of K₂O keeps depleting from the slag, it also indicates the transition of network structure from a floppy mode to rigid mode[25]. Additionally, it is also seen that not all K ions are concentrated in the channels or cations enriched region, a minor portion of K ions still penetrates into

the network for modification. This finding also reinforces the "perturbed network model" [26], which proposes that cations tend towards a more homogeneous distribution due to their interaction with bridging oxygens.

The short-range order information can be obtained from the calculated pair distribution function, where the Si-tetrahedron configuration is robust and modified by the network modifiers. The results are presented in Figures S1 to S6, and the bond length and coordination number results are listed in Table S2. The degree of polymerization in the tectosilicate network can be effectively described by the Qn index, which characterizes the Si tetrahedra based on their connection with 'n' bridging oxygen atoms, where 'n' ranges from 0 to 4. The computed average Q_n distribution of each slag is illustrated in Fig. 6(b). A more detailed Qn distribution can be seen in Table S3. As can be observed, the Q_n distribution is highly correlated with the SiO₂ content in the melt. Taking the KS-1 slag as an example, the average Q_n value increases from an initial value of 2.36 to 3.6. This observation aligns with the previously noted transformation of the tectosilicate structures from short chains to complex networks. As the initial K₂O content in the slag decreases, the range of Q_n values also gradually narrows. For instance, in the KCS-4 slag, the O_n value only transitions from 1.72 to 2.34, indicating that the final slag still maintains a good degree of depolymerization owing to the remaining CaO content.

As shown in Fig. 6(c), it is seen that the self-diffusion coefficient is strongly compositional dependent and decreases with the increase of SiO₂ content. For the ternary slags, at the same SiO₂ content, a higher $K_2O/(\text{CaO}+K_2\text{O})$ ratio leads to an increased diffusion coefficient. For instance, in the initial slag compositions, KCS-1 slag exhibits the highest average diffusion coefficient. This result also in good agreement with the measurements conducted by Chen and Zhao[27] where slag viscosity increases with lower $K_2O/(\text{CaO}+K_2\text{O})$. Therefore, it can be clearly seen that as the $K_2\text{O}$ -containing slag refining progresses, the conditions for mass transfer continuously deteriorate.

Given the inverse relationship between diffusivity and viscosity, the latter emerges as a useful indicator for assessing reaction kinetics. Based on the previous studies with confirmed equilibrium time of slag refining for B removal[10,28], a slag viscosity based empirical criterion can be employed to estimate whether the equilibria of B mass transfer from metal phase to slag phase has reached, as shown in Fig. 7. It is worth noting that even though the refining tests were conducted using different slag compositions and at different temperatures, the differences can be adequately compensated because slag viscosity is also sensitive to both factors[29,30] and thus correlates with kinetics. To achieve system equilibrium within a refining time of two hours, the slag viscosity needs to be around 0.25 Pa·s.

The viscosity of slags studied in this work is also calculated and results as detailed in Table S4. In the case of binary slag KS-1, the viscosity dramatically escalates from an initial 0.10 Pa·s to a final 6.63 Pa·s. Similarly, the binary slag KS-2 also experiences the rapid viscosity increase from 2.51 Pa·s to 9.37 Pa·s. In ternary slags, viscosity also increases as the K_2O content decreases. For the slag KCS-4 slag, which is with the least K_2O content, its viscosity varies from 0.08 Pa·s to 0.35 Pa·s. Thus, it can be inferred that the KSC-4 slag may reasonably reach or come close to the equilibrium at the end of refining. The binary slags are more likely to experience stagnation in mass transfer due to the high viscosity, and hence not solely thermodynamically driven.

4.2.2. Oxygen local environment and slag chemistry

An oxygen-centric view of slag melts presents three types of oxygen atoms in the system, respectively, bridging oxygen (BO), non-bridging oxygen (NBO), and free oxygen (FO). Based on the final composition of the slag, the distribution of these oxygen species is shown in Fig. 8(a). It can be seen that the bridging oxygen holds a predominant position in the binary system, while the proportion of NBO increases with the increase of CaO in the ternary system. For instance, the NBO percentage in KCS-4 reaches as high as 58.4, indicating that this slag melt has more

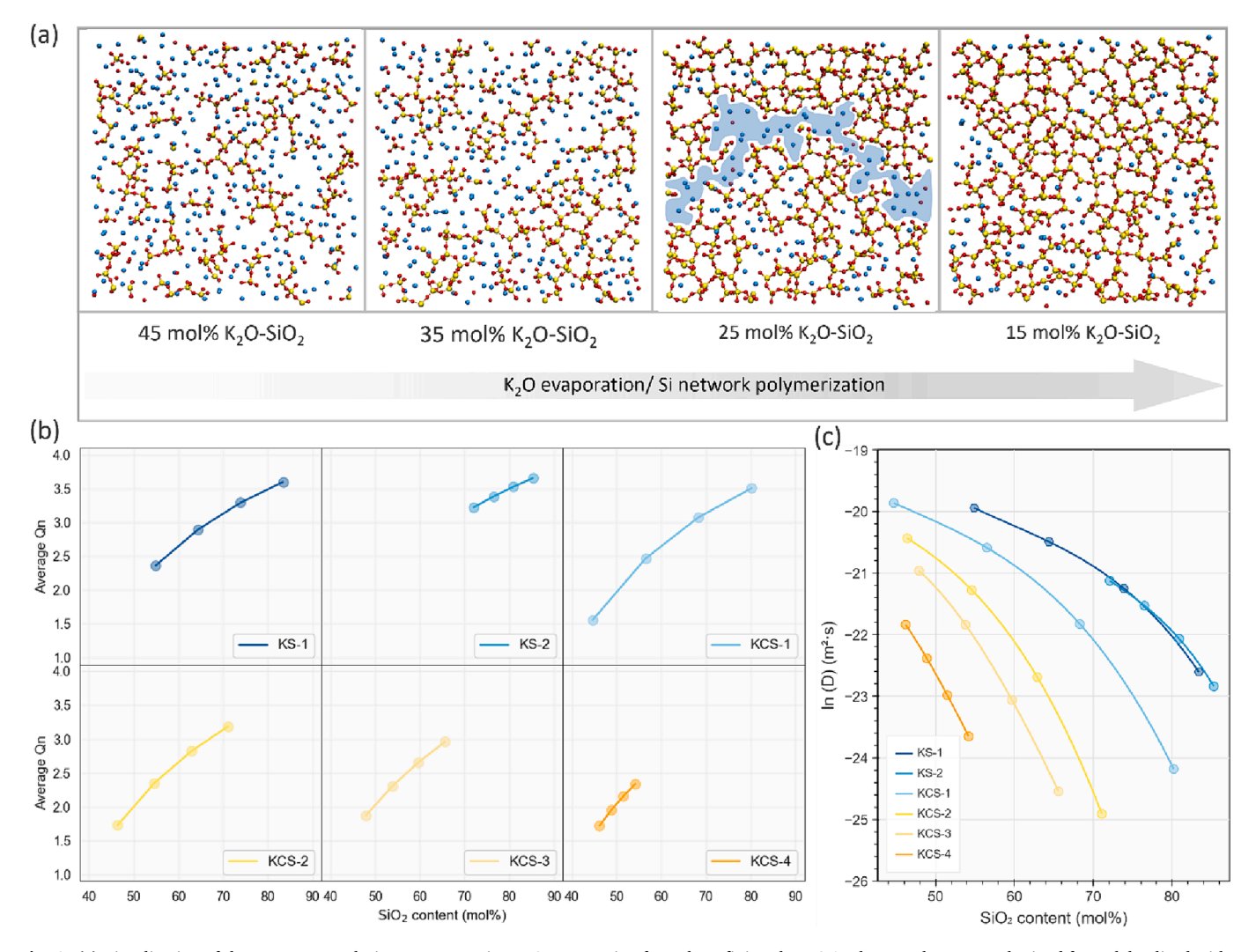


Fig. 6. (a) Visualization of slag structure evolution accompanying K_2O evaporation from the refining slag KS-1. The snapshots were obtained from slabs sliced with a thickness of 6 Å. In the images, K atoms are represented in blue, Si atoms in yellow, and O atoms in red. The area shaded in blue represents the observed percolation channel among the giant network components. (b) Variation of Q_n index of each slag. (c) Calculated average diffusion coefficient of slags with the increase in SiO_2 content. (For interpretation of the references to colour in this figure legend, the reader is referred to the web version of this article.)

reactive sites compared to other slag systems. Moreover, as shown in Fig. 8(b), the specific Q_n distribution of the final composition of the slag exhibits a trend with increasing Q_2 species in the ternary slags. This marks the network depolymerization and is also beneficial for the better integration of B complexes into the slag structure[31].

In addition, the presence of a modified form of BO by cations, namely, M-BO, was also observed and also reported in other slag system [32]. Experimental evidence of such interaction between cations and BO has also been reported.[26,33] This type of oxygen are observed particularly in high SiO2 region and when the cations have low field strength, making it difficult to break the covalent BO bond. Instead, the formation of M-BO promotes additional negative charge transfer to the oxygen and weaken the Si-O Coulombic interactions, therefore weaken the Si-O-Si bond. As seen in Fig. 9, the bridging oxygen species modified by a single K ion, referred to as O-2Si(K), is the most abundant, followed by the bridging oxygen O-2Si(2 K) modified by two K ions, and even O-2Si(3 K) that one bridging oxygen modified by three K ions. Thus, the primary distribution of K ions in the slag is with the configuration of modified bridging oxygen M-BO. In the case of ternary slags, the primary form of M-BO is only the O-2Si(Ca) where a BO modified by a single Ca ion. Although K ions co-modifies oxygen ions with Ca ions, as the ratio of K2O/CaO decreases, the content of NBO species, such as O-Si (2Ca) and O-Si(3Ca), rapidly increases. It can be inferred that, compared to K ions, Ca ions demonstrate a heightened propensity for inducing the formation of NBO. Thus, the areas containing Ca ions in the slag melts are also more likely to exhibit an enrichment of NBO, which further aids the stabilization of acidic B_2O_3 units in the slags.

Interestingly, as shown in Fig. 10, further observation of the distribution of Ca and K ions in the slag melts reveals that they do not exhibit ideal mixing. The distribution of Ca and K ions can be compared by dividing the simulation box evenly into 5x5 squares along the y-z plane and projecting atoms along the x-axis onto the y-z plane. In the case of ideal mixing, within these 25 regions, the distribution percentage for each type of ion in each region should be equal, namely, at 4 %. However, as shown in Fig. 11, the distributions of Ca and K ions exhibit distinct characteristics of clustering. This implies that Ca and K ions tend to avoid coexisting in the same region, preferring instead to segregate into different areas. Similar behaviour also occurs between Ca and Na as reported by Cormier and Neuville [34]. The reason behind this phenomenon, as previously described, lies in the higher charge and greater field strength of Ca ions, which makes them more prone to causing the accumulation of NBO, indicating a preference for depolymerized regions. Conversely, K ions are more inclined to modify BO, forming M-BO, and therefore, K ions tend to appear in polymerized areas. Thus, it can also be understood that the ternary K2O-CaO-SiO2 refining slag should combine the characteristics of both K2O-SiO2 and CaO-SiO2 slag

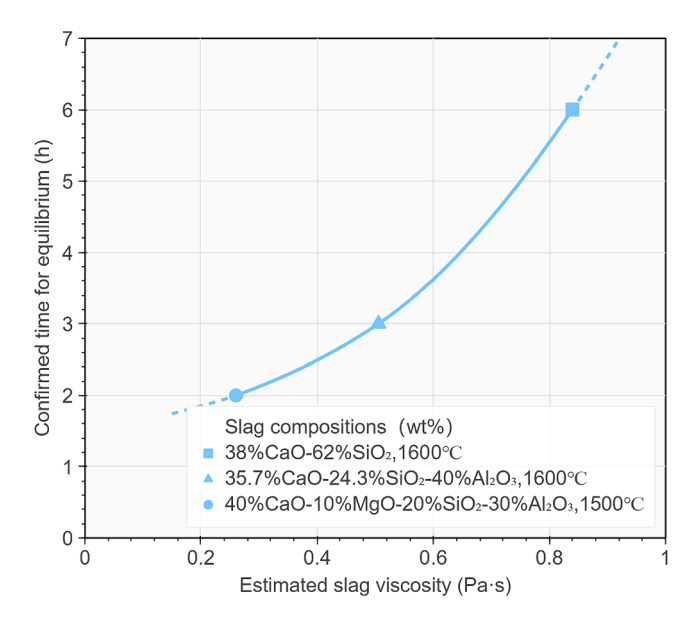


Fig. 7. Empirical relationship between slag viscosity and time required to reach equilibria for B distribution between the slag and silicon. The slag viscosity was calculated by FactSage 8.1[22].

systems, which implies that it possesses distinct B removal mechanisms. This will be further discussed in the following section.

4.3. Boron removal and distribution

4.3.1. Boron removal degree

The B concentration in the Si phase changes significantly after the refining experiments. As indicated by the ICP-MS measurement, the final B concentration in Si lies between 4.2 and 7.3 ppmw. Based on its concentration in the Si phase before and after the experiments, the B removal degree is calculated using the following formula:

$$B \ removal \ degree = \frac{m_{\text{Si}}^{\text{initial}} C_{\text{B in Si}}^{\text{initial}} - m_{\text{Si}}^{\text{final}} C_{\text{B in Si}}^{\text{final}}}{m_{\text{Si}}^{\text{initial}} C_{\text{B in Si}}^{\text{initial}}} \times 100\%$$
(7)

As illustrated in Fig. 12, all the slags demonstrate effective B

removal. Taking into account the mass decrease in the metal phase due to the silicothermic reduction reaction, the corrected B removal degree shows more accurate value and higher than the value calculated with the assumption of a constant metal phase mass. Notably, the actual B removal percentages ranging from 74.4 % of KCS-2 slag to 84.9 % of KCS-1 slag.

4.3.2. Boron distribution

In the conventional slag refining, B can either be distributed in the slag phase or the metal phase. However, the presence of alkali metal oxides in the slag provides an alternative pathway for B removal, namely the formation of volatile compounds that remove B through evaporation. Therefore, in the present work, it is crucial to investigate the distribution of B elements after refining experiments. By analysing the measured B composition in both the slag and metal phases before and after refining, the net mass loss of B from the system can be attributed to B loss through evaporation. Thus, the final B distribution percentage was plotted as shown in Fig. 13.

The results indicate that the initial Si raw material is the primary contributor of B in the entire refining system, accounting for approximately 70 % or more of the total B present. The initial B content in the slag phase for all six samples ranges from 13.1 % to 31.7 %. Furthermore, it is also seen that the B content in the initial slag phase decreases with decreasing K_2O content, which is due to the K_2O slag raw material containing a certain amount of B or potential contamination through the slag preparation.

After the refining tests, a significant change in B distribution was observed. The final refined Si phase contains the least B content as opposed to being the highest before refining. It ranges from only 12.4 % to 21.5 %. The percentage of evaporated B from each sample varied widely, with KCS-1 having the highest percentage of evaporated B (61.8 %) but the lowest B content in slag (25.8 %), while KCS-4 had the lowest B evaporation (14.3 %), but the highest B content in the slag phase (67.7 %). Moreover, it can be observed that although most of the B is removed in gaseous form in the binary slag systems KS-1 and KS-2, there are still a substantial amount of B remains in the slag phase. Thus, above all, these B distribution results provide valuable insights into B removal during slag refining and emphasizing the importance of B evaporation directly due to the addition of K_2O in the slags.

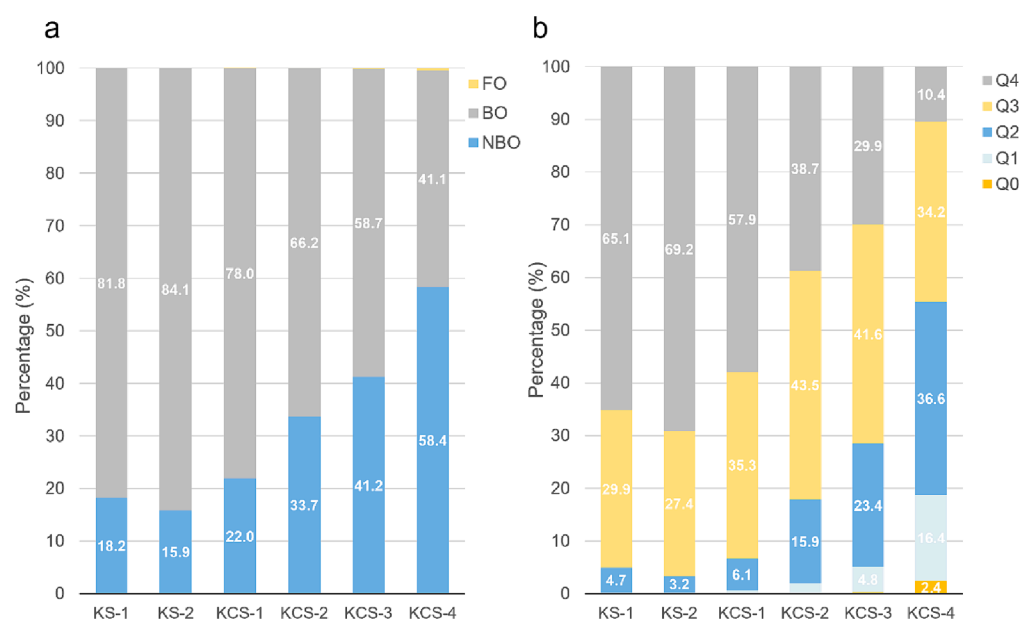


Fig. 8. Percentage of oxygen types (left) and specific Q_n distribution (right) of the slag compositions at the end of refining.

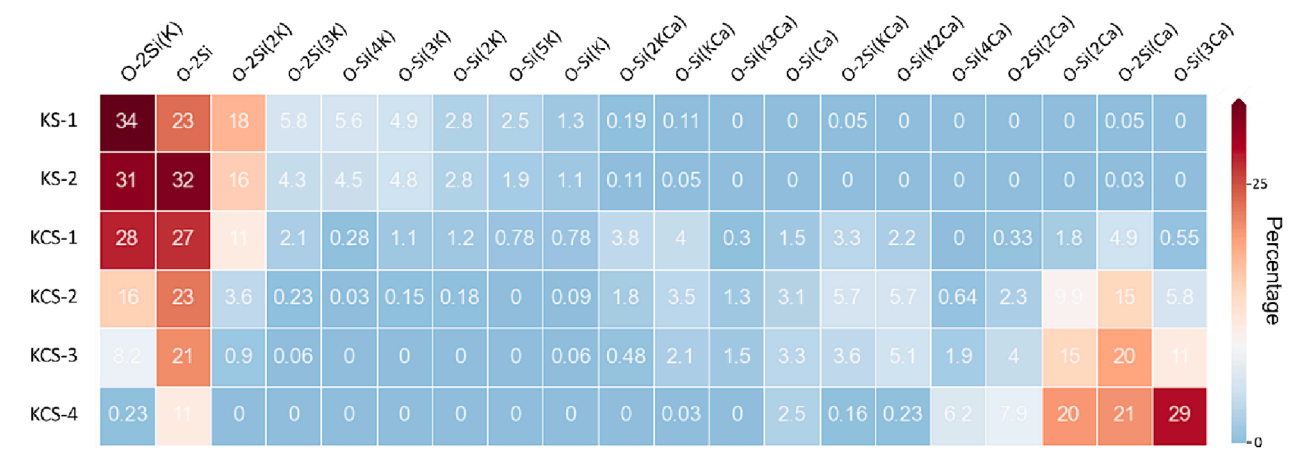


Fig. 9. Microscopic local environment of oxygen species obtained from MD simulation of the slag compositions at the end of refining.

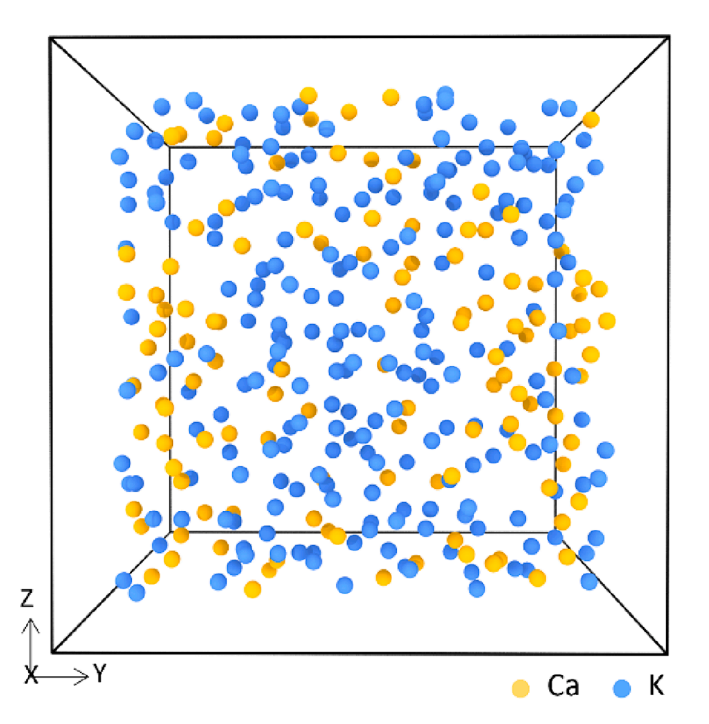


Fig. 10. A snapshot of the non-ideal mixing of Ca and K ions in the KCS-3 slag before slag refining, with a composition of 23.4 mol% K_2O , 28.7 mol% CaO, 47.9 mol% SiO_2 . The snapshot is parallel to the y-z plane and has a slab thickness of 10~Å.

4.3.3. Boron removal mechanism

B removal from the Si phase occurs at the slag/Si interface and proceeds through the following stages: first, the mass transfer of dissolved boron in liquid silicon towards the boundary layer of the interface. Subsequently, the oxidation of boron into B_2O_3 takes place at the

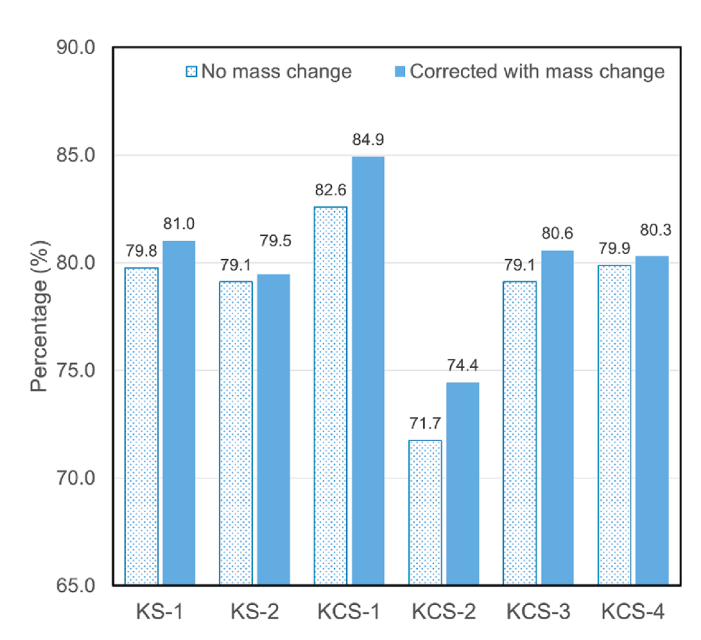


Fig. 12. Results of B removal percentage from Si phase.

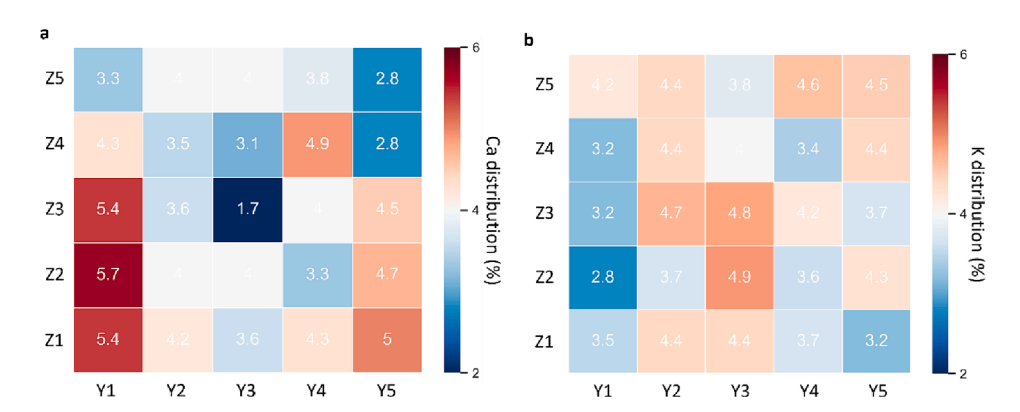


Fig. 11. Spatial distribution percentage of network modifiers in the initial KCS-3 slag melt obtained by dividing the y-z plane into 5x5 square regions and projecting atoms along the x-axis onto the y-z plane, where ideal mixing would result in each region containing 4% of ions: (a) distribution of Ca ions; (b) distribution of K ions.

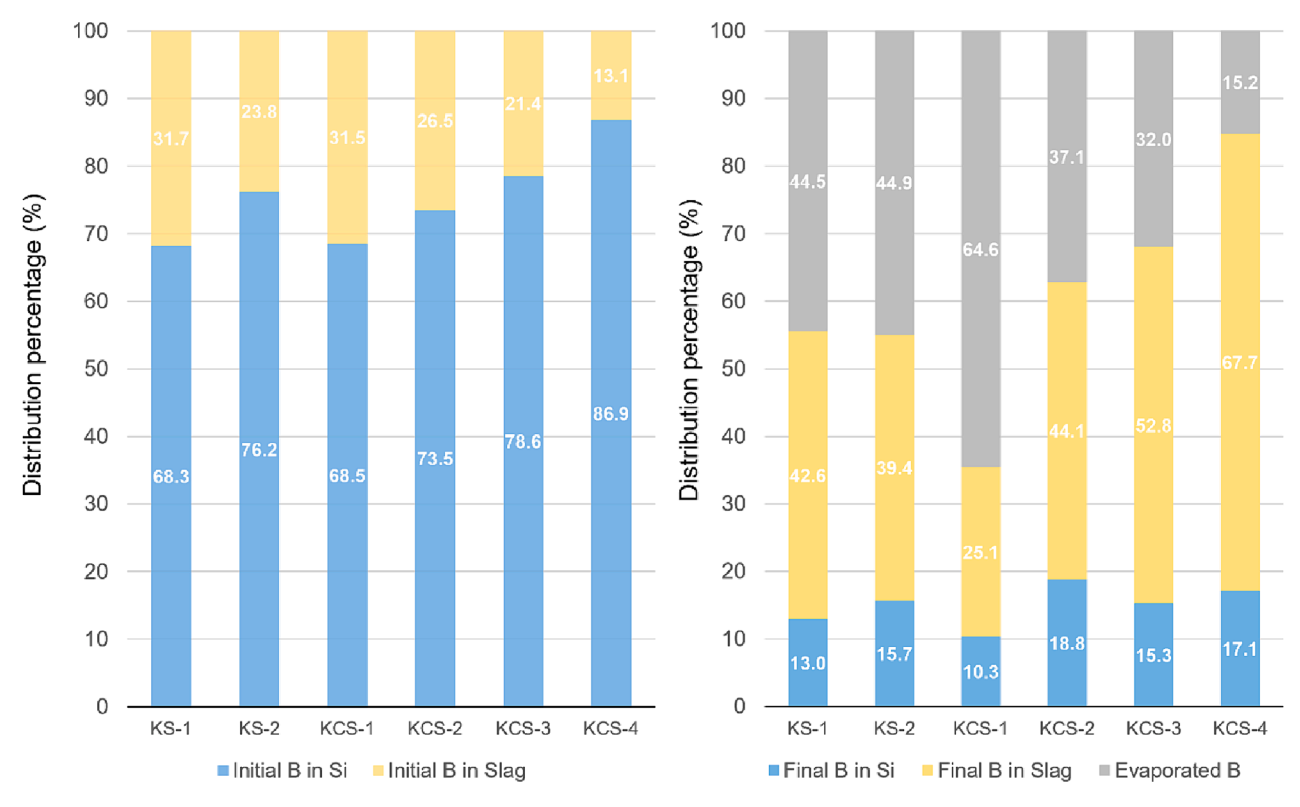


Fig. 13. Boron distribution in different phases before (left) and after (right) slag refining.

interfacial area. Further, the transferred B is removed via the formation of volatile species or transferred into the deeper regions of the slag phase. In the present work of K_2O -CaO-SiO $_2$ slag system, the possible reactions involving B oxidation of the oxides can be listed as below:

$$\frac{3}{4}(SiO_2) + [B] = \frac{3}{4}Si + \frac{1}{2}(B_2O_3) \tag{8}$$

$$\frac{3}{2}(K_2O) + [B] = 3[K] + \frac{1}{2}(B_2O_3)$$
 (9)

$$\frac{3}{2}(\text{CaO}) + [\text{B}] = \frac{3}{2}[\text{Ca}] + \frac{1}{2}(\text{B}_2\text{O}_3) \tag{10}$$

The relevant standard Gibbs free energy of the reactions is then expressed as:

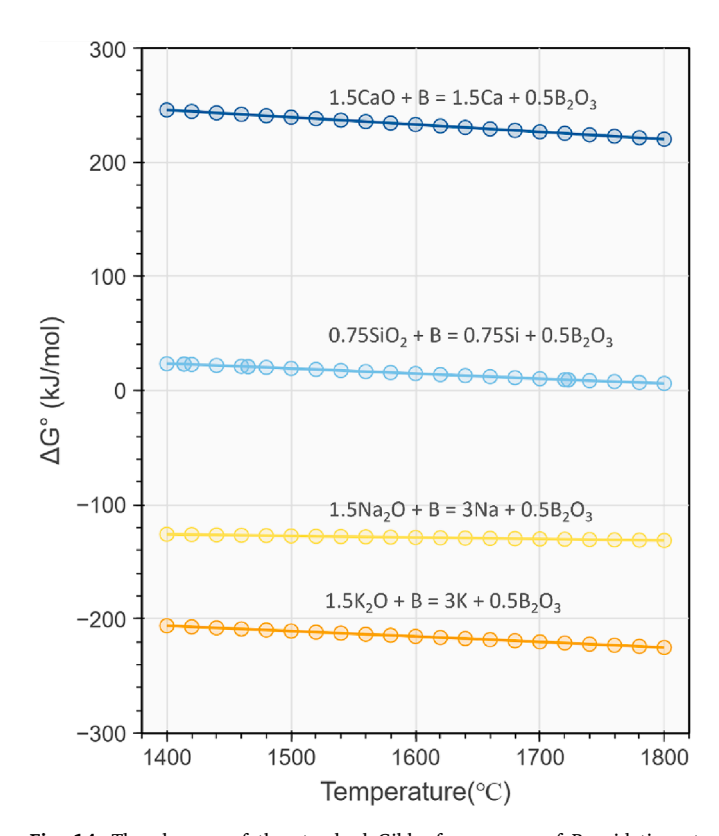
$$\Delta G_8 = \Delta G_8^{\circ} + RT \ln \left(\frac{a_{Si}^{3/4} a_{B_2O_3}^{1/2}}{a_B a_{SiO_2}^{3/4}} \right)$$
 (11)

$$\Delta G_9 = \Delta G_9^{\circ} + RT \ln \left(\frac{a_K^3 a_{B_2 O_3}^{1/2}}{a_B a_{K_2 O}^{3/2}} \right)$$
 (12)

$$\Delta G_{10} = \Delta G_{10}^{\circ} + RT \ln \left(\frac{a_{Ca}^{3/2} a_{B_2 O_3}^{1/2}}{a_B a_{CaO}^{3/2}} \right)$$
 (13)

The standard Gibbs free energy of the aforementioned reactions can be obtained from the FTlite and FToxid data in FactSage 8.1, as illustrated in Fig. 14. In the previous study of $Na_2O\text{-}SiO_2$ refining system by Safarian et al.[12], it has been thermodynamically confirmed that B oxidation is much more favourable by Na_2O rather than SiO_2 . Thus, it is also necessary to compare the two alkali slag refining systems and the following reaction is also included.

$$\frac{3}{2}(Na_2O) + [B] = 3[Na] + \frac{1}{2}(B_2O_3)$$
 (14)



 ${f Fig.~14.}$ The changes of the standard Gibbs free energy of B oxidation at varying temperature.

$$\Delta G_{14} = \Delta G_{14}^{\circ} + RT \ln \left(\frac{a_{Na}^{3} a_{B_{2}O_{3}}^{1/2}}{a_{B} a_{Na,O}^{3/2}} \right)$$
 (15)

The plotted diagram for B oxidation demonstrates the Reaction (9) has the lowest standard Gibbs free energy, indicating that the oxidation reaction involving K_2O is the most thermodynamically favourable under standard condition where pure substance participates in the reaction. However, since the slag refining system is under non-standard condition with mixed liquid solution, the actual situation will still exhibit discrepancies.

Although accurate activity values for B and B_2O_3 are difficult to obtain, which makes the non-standard Gibbs free energy of the aforementioned reactions cannot be calculated, considering the B related terms yielded consistent values for a single refining system, through the rearrangement of the above equations we obtain:

$$\delta G_8 = \Delta G_8 - RT \ln \left(\frac{a_{B_2O_3}^{1/2}}{a_B} \right) = \Delta G_8^{\circ} + RT \ln \left(\frac{a_{Si}^{3/4}}{a_{SiO_2}^{3/4}} \right)$$
 (16)

$$\delta G_9 = \Delta G_9 - RT \ln \left(\frac{a_{\text{B}_2 \text{O}_3}^{1/2}}{a_{\text{B}}} \right) = \Delta G_9^{\circ} + RT \ln \left(\frac{a_{\text{K}}^3}{a_{\text{K},\text{O}}^{3/2}} \right)$$
 (17)

$$\delta G_{10} = \Delta G_{10} - RT \ln \left(\frac{a_{\text{B}_2\text{O}_3}^{1/2}}{a_{\text{B}}} \right) = \Delta G_{10}^{\circ} + RT \ln \left(\frac{a_{\text{Ca}}^{3/2}}{a_{\text{Ca}}^{3/2}} \right)$$
(18)

It can be observed that after eliminating the effects of the B related terms, the relative magnitudes of δG_{10} , δG_{11} , and δG_{12} on the left-hand side can be employed to evaluate the boron oxidation capacity of different oxidants under non-standard states. Accordingly, for comparison, we also have the expression for Na₂O slag system:

$$\delta G_{14} = \Delta G_{14} - RT \ln \left(\frac{a_{\text{B}_2\text{O}_3}^{1/2}}{a_{\text{B}}} \right) = \Delta G_{14}^{\circ} + RT \ln \left(\frac{a_{\text{Na}}^3}{a_{\text{Na}_2\text{O}}^{3/2}} \right)$$
(19)

Fig. 15 presents the calculated δG values corresponding to each oxidation reaction in the following binary slag refining systems K_2O -SiO₂, Na₂O-SiO₂, and CaO-SiO₂ at 1600 °C. For ease of comparison, the metal content in the Si melt is set at the maximum measured value of 5000 ppmw. The activity values for the different slag systems are obtained from the FToxid database in FactSage 8.1, while the activity values in the metal phase are computed using the FTlite database.

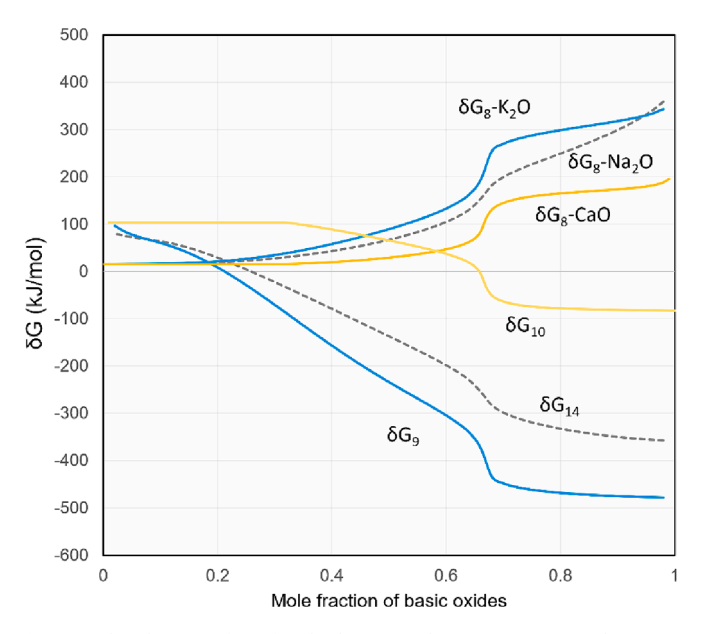


Fig. 15. The changes of δG for the boron oxidation reactions, with varying binary slag composition and given the metal concentration in Si as 5000 ppmw.

It can be observed that in the $K_2O\text{-SiO}_2$ refining system, the δG_{11} curve corresponding to K_2O oxidation exhibits the lowest values, indicating that K_2O provides the primary driving force for B removal. Although we cannot directly compare the absolute values of δG for the oxidation reactions of K_2O and Na_2O due to the different activities of B_2O_3 , it is evident that the larger difference of K_2O curve with SiO_2 curve in the $K_2O\text{-SiO}_2$ slag system as compared to the difference of Na_2O with SiO_2 in the $Na_2O\text{-SiO}_2$ slag system suggests a more dominant role for the oxidation reaction of K_2O with B in the $K_2O\text{-SiO}_2$ system. Moreover, through the $CaO\text{-SiO}_2$ system, it can be seen that the primary driving force for B oxidation is more related to the slag basicity, with high basicity dominated by CaO and low basicity dominated by CaO and low basicity dominated by CaO and CaO by CaO by CaO and CaO by CaO by CaO by CaO and CaO by CaO by

The δG values variation in ternary $K_2O\text{-CaO-SiO}_2$ is presented in Fig. 16. For the sake of comparison, the SiO_2 content was fixed at 50 mol %. It can be observed that throughout almost the entire range, K_2O predominantly governs the oxidation potential of B. However, as the K_2O content in the slag decreases, there is a gradual transition to SiO_2 dominance. It is then expected that during the early stages of the real slag refining process, the removal of B is primarily governed by K_2O . However, after substantial depletion of K_2O , the significant increase in SiO_2 content will dictate the subsequent B removal and more controlled by reaction equilibrium and kinetics condition.

As discussed in the B distribution, it is known that after B is oxidized and incorporated into the slag, the produced B_2O_3 will continue to react with K_2O present in the slag, leading to the formation of volatile compounds. The possible reactions to convert boron oxide into the gaseous phase can be written as:

$$(B_2O_3) = B_2O_3(g)$$
 (20)

$$\frac{1}{2}(K_2O) + (B_2O_3) = \frac{1}{2}K_2B_4O_7(g) \tag{21} \label{eq:20}$$

$$\frac{1}{2}(K_2O) + \frac{1}{2}(B_2O_3) = KBO_2(g)$$
 (22)

Similarly, as presented in Fig. 17, it is observed that B_2O_3 direct evaporation is not possible from thermodynamics point of view, whereas the formation of potassium metaborate (KBO₂) emerges as the most favourable pathway for B evaporation. Furthermore, as shown in Fig. 18, the possible distribution of gaseous species under the refining conditions of slag KCS-1 was investigated through FactSage calculations

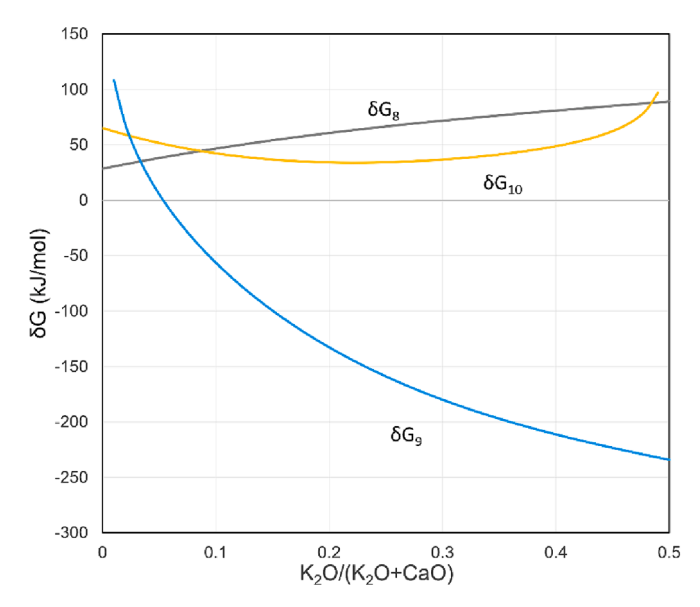


Fig. 16. The changes of δG for the boron oxidation reactions in the ternary K_2O -CaO-50 mol%SiO₂ slag system, with varying $K_2O/(K_2O+CaO)$ ratio and given the metal concentration in Si as 5000 ppmw.

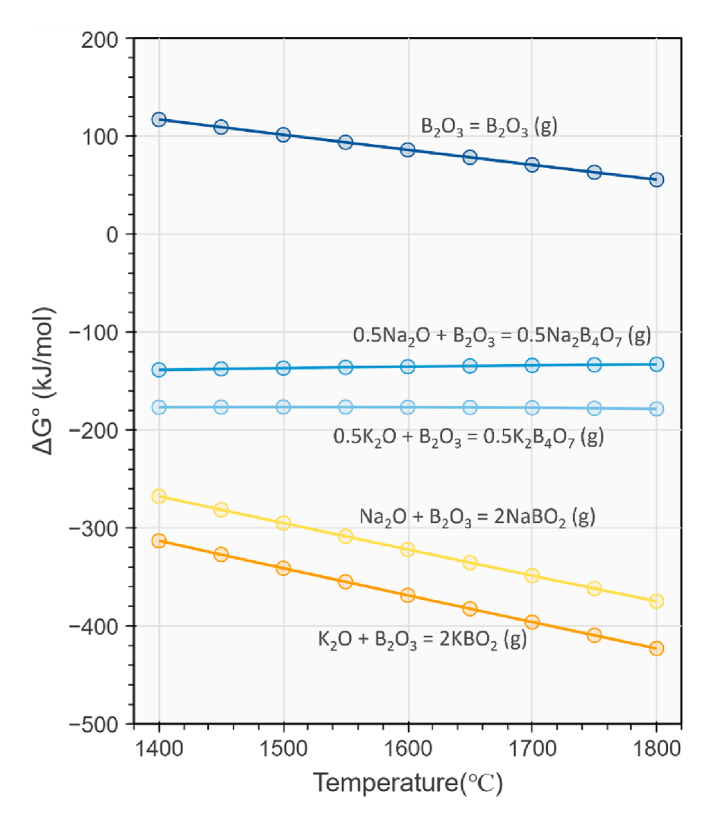


Fig. 17. The changes of the standard Gibbs free energy of B gasification at varying temperature.

by employing the Effective Equilibrium Reaction Zone (EERZ) method. For simplicity, the diffusion rate of all elements within each phase, namely slag and alloy, was presumed to be identical. It is also seen that

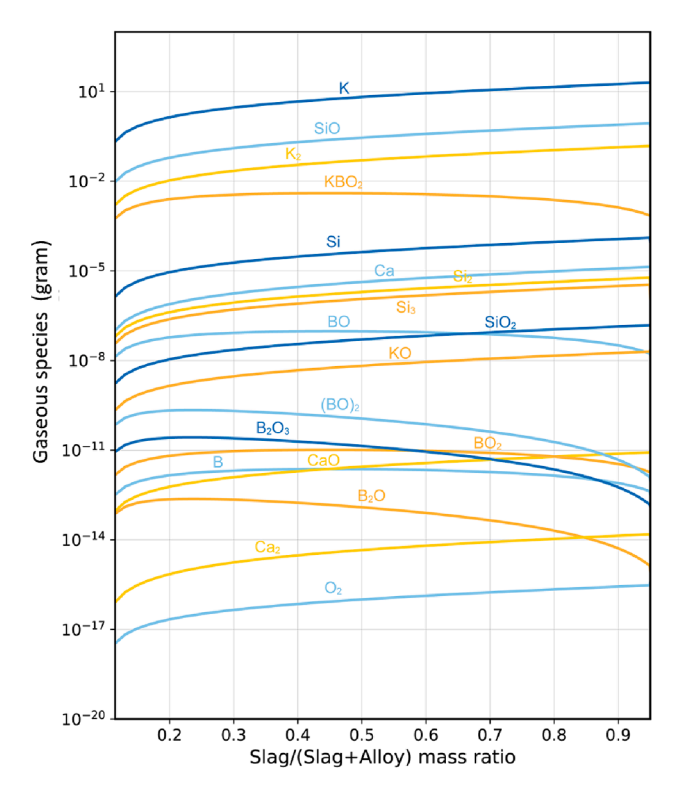


Fig. 18. Gaseous species distribution under the refining conditions for slag KCS-1, calculated by FactSage using the effective equilibrium reaction zone method.

the gaseous species KBO_2 prevails for all possible B-containing gaseous composition combinations in the local effective reaction zone. This is also in agreement with the B distribution results that K_2O content directly related to the degree of B gasification. Thus, considering the above discussions, the B removal mechanisms and main mass transport in the K_2O slag refining systems is illustrated in Fig. 19.

4.3.4. L_B value

The B distribution coefficient also known as partition ratio is widely used to evaluate the extent of B removal by slag refining, which is given by:

$$L_{\rm B} = \frac{(\%B)}{[\%B]} \tag{23}$$

where (%B) and [%B] is the B concentration in slag and Si phase, typically in wt%.

The calculated L_B results are presented in Fig. 20 and compared with literature data in Fig. 21. The obtained L_B values in this work vary from a minimum value 1.4 for slag KCS-2 to a maximum value of 2.28 for KCS-4. Notably, the numbers for KCS-4 and KCS-3 are in good agreement with the results obtained by Jakobsson [28]. Furthermore, it is also seen that the L_B of the KS-1 slag is exceeding the 1.5 of KS-2 slag that with similar final composition. Based on previous discussions on viscosity and equilibrium time, the high L_B of KS-1 is likely be attributed to the initial slag composition containing higher content of K2O. This led to a substantial aggregation of B at the interfacial area in the early stages of refining. The subsequent sharp increase in viscosity resulted in a stagnation of mass transfer, thereby maintaining the high L_B until the end of refining. Similarly, the higher L_B of KCS-1 slag to KCS-2 can also be explained. Thus, since both a high initial K₂O content and a high CaO content in the slag can promote an increasing L_B value, the KCS-2 with intermediate composition corresponds to the lowest LB value.

Based on the results above, it is evident that the K_2O -CaO-SiO₂ ternary slag system possesses a unique advantage by integrating two different boron removal mechanisms: the gasification of boron during the early refining stage and the B redistribution based on chemical equilibrium in the later stage. This also implies that the boron removal capability of the CaO-SiO₂ slag system can be further enhanced by the addition of K_2O , facilitating the production of higher purity silicon. Considering the current industrial slag refining practices, the introduction of a small amount of alkali slag for boron gasification in highly basic

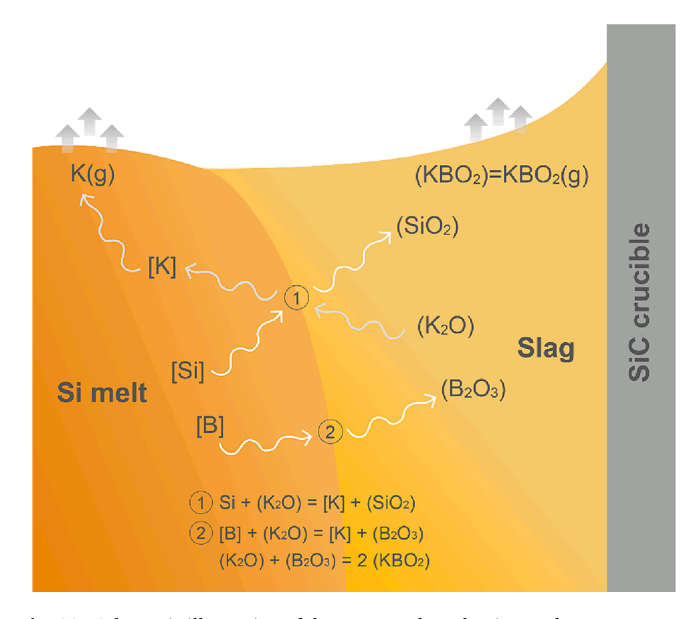


Fig. 19. Schematic illustration of the B removal mechanism and mass transport in the studied K₂O slag refining system.

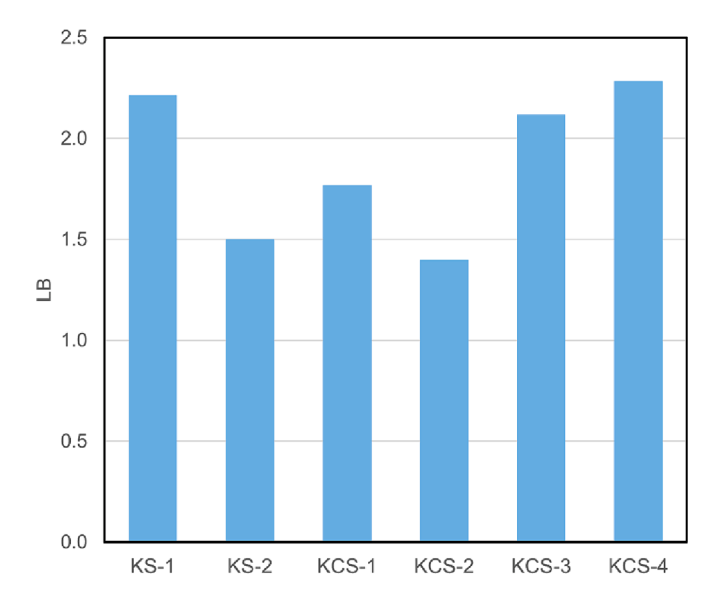


Fig. 20. B distribution coefficient (LB) between slag and silicon phase.

alkaline earth slag systems should present a more practical route, as it does not require significant equipment modifications.

4.4. Mechanism of Si-kerf recycling

As shown in Fig. 22, the covered $\mathrm{Si}_x\mathrm{O}_y$ oxidation layer on Si powders makes the recycling of Si-kerf waste challenging. However, with the presence of basic oxides such as $\mathrm{K}_2\mathrm{O}$ and CaO , the oxide layer could be dissolved. The liberated Si droplets subsequently coalesce and integrate into the Si melt to attain the recovery of Si.

Another challenge in kerf recycling is the separation of SiC from Si. Since SiC and silicon share similar physicochemical properties, it is difficult to directly separate them from the kerf waste. However, according to the research by Safarian et al.[38], SiC exhibits superior wettability with liquid slag compared to that between liquid slag and Si melt. This suggests that SiC can be more readily absorbed by the slag phase. Moreover, based on the Leenov-Kolin's theory[39], when a conductive melt is compressed by the electromagnetic force and a pressure gradient is induced. In response, the suspended particles receive a force that moves them oppositely towards the liquid vicinity.

This force is expressed as:

$$F_P = -\frac{3}{4} \frac{\pi d_p^3}{6} F \tag{24}$$

where F_P is the force acting on the SiC particle, F indicates the imposed electromagnetic force, and d_P represents the particle diameter.

In the case of the present work, the removal mechanism of SiC emerges as a multi-stage process. As illustrated in Fig. 22, initially, the SiC particles are transported towards the Si/slag interface due to the electromagnetic induction. Subsequently, the SiC particles overcome the rebound force of the silicon/Slag interface to further transported into the slag phase.

The wetting behaviour of the liquid slag and SiC particle plays an important role when SiC particles pass through the slag-metal interface. In general, for an inert system with ideal solid surface, the wettability can be evaluated by the contact angle using the Young's equation, which defined as:

$$cos\theta = \frac{\gamma_{SG} - \gamma_{LS}}{\gamma_{LG}} \tag{25}$$

where γ_{SG} and γ_{LG} indicate surface tension of solid and liquid phase, respectively, and γ_{LS} represents solid–liquid interfacial energy. It is commonly accepted that a liquid has contact angle $< 90^{\circ}$ refers as wetting liquid while $> 90^{\circ}$ the non-wetting liquid.

The estimated wetting contact angle of SiC and slag ($\theta_{SiC/slag}$), ranging from 25° to 30° as shown in Fig. 3, along with the higher value for the Si melt and SiC ($\theta_{SiC/Si}$) between 38 and 40°, demonstrates that SiC particles are wetted better by the slag melts than by the metal phase. The improved wetting between slag and SiC can be attributed to multiple factors, while one of the most important reasons might be the chemical reactions occurring in the system. The interfacial reactions can significantly enhance wetting and the smallest contact angle can be represented by the following equation[40]:

$$cos\theta_{min} = cos\theta_0 - \frac{\Delta \gamma_r}{\gamma_{LG}} - \frac{\Delta G_r}{\gamma_{LG}}$$
(26)

where θ_0 is the contact angle on the substrate without any reaction and $\Delta \gamma_r$ represents the change of interfacial energy due to reaction and ΔG_r is the change in free energy per unit area at the interface.

Although those quantities are difficult to obtain in a reactive interface system, it has been evidenced by Safarian et al. [38] that gaseous products were formed along the interface of SiC and CaO-SiO_2 slags due to following chemical reaction occurred along the interface.

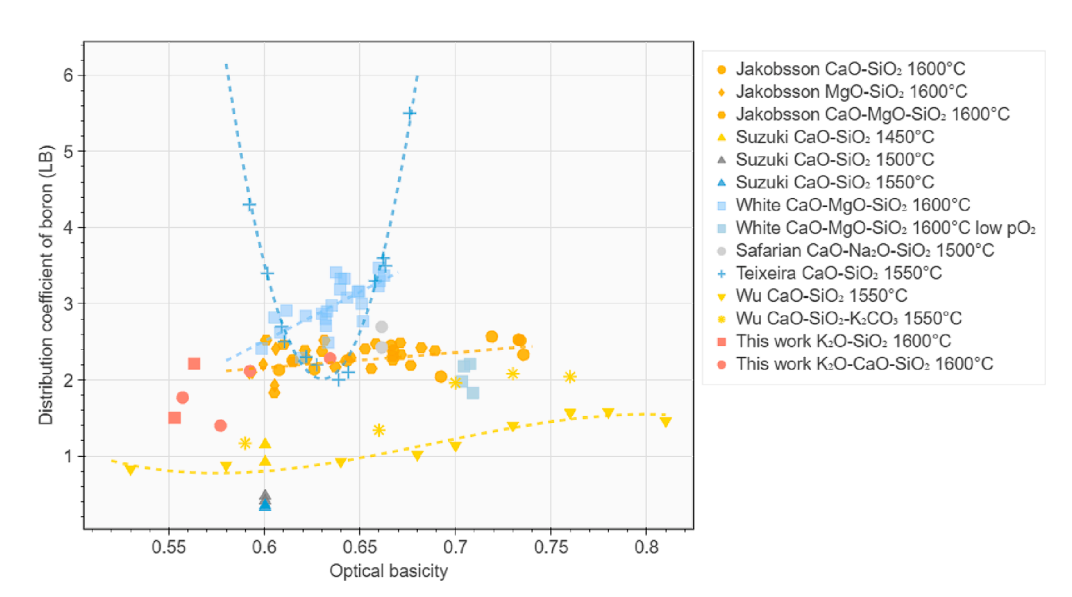


Fig. 21. Comparison of boron distribution coefficient from the present work literature data across various silicate slag systems [8,10,11,16,28,35-37].

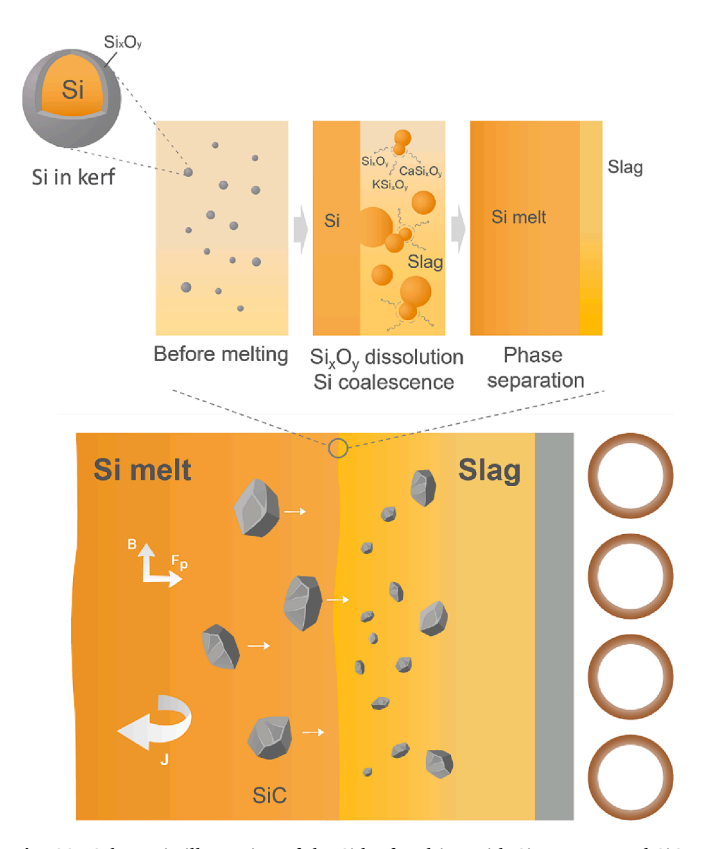


Fig. 22. Schematic illustration of the Si-kerf melting with Si recovery and SiC separation process at the silicon/slag interface.

$$SiC^{surf} + (SiO_2) = SiO(g) + CO(g)$$
(27)

Similar observation was also reported by Li et al. [41] as gas bubble formed on the SiC particles, which resulted in a rough surface. It is also known that the wear of SiC bricks can be deteriorated by the erosion of alkali elements, leading to the formation of various silicates [20] Take consideration of the currently studied K_2O -CaO-SiO $_2$ system, the following reactions might be possible between SiC and K_2O , which can be represented as:

$$(K_2O) + xSiC^{surf} + 3x(O) = K_2O \bullet xSiO_2^{surf} + xCO(g)$$
(28)

$$(K2O) + SiCsurf = SiO(g) + CO(g) + 2[K]$$
(29)

Hence, the interfacial reaction should play an important role in enhancing the SiC particle wetting in the slag melts. Notably, the wettability can also be further enhanced due to resultant rough surface of the chemical reactions as the solid–liquid interfacial area increases.

Additionally, according to the experimental and theoretical investigation of Kadkhodabeigi et al. [42] and Li et al. [43] the separation of SiC particles into slag phase is facilitated by larger particle size, prolonged time, and higher temperature. Similar patterns can also be observed from Fig. 4(a), where larger SiC particles are distributed further from the interface, while smaller SiC particles are located near the interface. Thus, the SiC removal, as determined in this study, appears to be an intricate interplay of physical and chemical processes.

5. Conclusions

In this study, the compositional effects on combined boron removal and kerf recycling through binary $K_2O\text{-}SiO_2$ and ternary $K_2O\text{-}CaO\text{-}SiO_2$ slags at 1600°C were investigated. The findings and conclusions can be summarised as follows:

- 1. The mass loss in the examined slag refining systems increases linearly with increasing $\rm K_2O$ content, from 8.8 % at 12.1 mol% $\rm K_2O$ to 20.6 % at 43.9 mol% $\rm K_2O$ in the ternary slags. Further mass balance analysis reveals two primary mechanisms for K loss from the melts: direct evaporation from the slag and the evaporation of metallic K from Si melt, which results from the silicothermic reduction of $\rm K_2O$. The latter is more pronounced in ternary systems, where the percentage of K lost surges from 33.8 % to 90.6 % as the $\rm K_2O$ content increases from 12 mol% to 44 mol%.
- 2. The reduction of K_2O content from slag phase led to significant deterioration of slag transport properties and limited mass transfer, especially in binary K_2O -SiO $_2$ slags.
- 3. Evidence from molecular dynamics simulations highlights that in the high SiO₂ region, K cations exhibit a propensity to modify bridging oxygen without breaking the Si-O-Si linkage to form the non-bridging oxygen. Meanwhile, Ca cations tend to depolymerize the tectosilicate network and create more non-bridging oxygen, which in turn promotes the stabilization of B within the slag phase.
- 4. Boron removal degree was approximately 80 % across all tests, with gasification through evaporation of potassium metaborate at slag/Si interface confirmed as an important removal mechanism, which is particularly dominant in high K_2O slags. Increasing CaO in slags enhances boron partitioning. However, high K_2O content also results in boron retention in the slag, reinforced by a marked rise in viscosity preventing its return to the Si phase.
- 5. The experimental work demonstrates that the recycling of Si-kerf is feasible when combined with the slag refining process. The formation of a substantial and homogeneous Si metal phase marks the successful oxidation layer removal and well remelting of the Si-kerf powders. The presence of SiC clusters in slag phase was observed, indicating effective removal of SiC and the feasibility of Si-kerf waste recycling.

CRediT authorship contribution statement

Mengyi Zhu: Writing – review & editing, Writing – original draft, Visualization, Validation, Software, Methodology, Investigation, Formal analysis, Conceptualization. Guixuan Wu: Writing – review & editing, Validation, Software, Resources. Kai Tang: Writing – review & editing, Software. Michael Müller: Writing – review & editing, Supervision, Resources. Jafar Safarian: Writing – review & editing, Validation, Supervision, Resources, Project administration, Methodology, Funding acquisition, Conceptualization.

Declaration of competing interest

The authors declare that they have no known competing financial interests or personal relationships that could have appeared to influence the work reported in this paper.

Data availability

Data will be made available on request.

Acknowledgement

This work was performed at Norwegian University of Science and Technology (NTNU) within the Research Centre for Sustainable Solar Cell Technology (FME SuSolTech, Project No. 257639), co-sponsored by the Norwegian Research Council and industry partners. Simulations were performed with computing resources granted by RWTH Aachen University under Project p0200350.

Appendix A. Supplementary data

Supplementary data to this article can be found online at https://doi.

org/10.1016/j.cej.2024.150788.

References

- [1] Solar PV, IEA, Paris, (2022). https://www.iea.org/reports/solar-pv.
- [2] K. Wei, S. Yang, X. Wan, W. Ma, J. Wu, Y. Lei, Review of silicon recovery and purification from saw silicon powder, JOM 72 (2020) (1989) 2633–2647, https:// doi.org/10.1007/s11837-020-04183-8
- [3] J. Safarian, G. Tranell, M. Tangstad, Processes for upgrading metallurgical grade silicon to Solar grade silicon, Energy Procedia 20 (2012) 88–97, https://doi.org/ 10.1016/j.egypro.2012.03.011.
- [4] L.K. Jakobsson, M. Tangstad, Thermodynamics of boron removal from silicon using CaO-MgO-Al2O3-SiO2 slags, Metall and Materi Trans b. 49 (2018) 1699–1708, https://doi.org/10.1007/s11663-018-1250-7.
- [5] M. Zhu, A. Azarov, E. Monakhov, K. Tang, J. Safarian, Phosphorus separation from metallurgical-grade silicon by magnesium alloying and acid leaching, Sep. Purif. Technol. 240 (2020) 116614, https://doi.org/10.1016/j.seppur.2020.116614.
- [6] M. Zhu, S.Y. Yue, K. Tang, J. Safarian, New insights into silicon purification by alloying-leaching refining: a Comparative study of Mg–Si, Ca–Si, and Ca–Mg–Si systems, ACS Sustainable Chem. Eng. 8 (2020) 15953–15966, https://doi.org/ 10.1021/acssuschemeng.0c05564.
- [7] L.A.V. Teixeira, Y. Tokuda, T. Yoko, K. Morita, Behavior and state of boron in CaO—SiO2 slags during refining of Solar grade silicon, ISIJ Int. 49 (2009) 777–782, https://doi.org/10.2355/isiiinternational.49.777.
- [8] L.A.V. Teixeira, K. Morita, Removal of boron from molten silicon using CaO-SiO2 based slags, ISIJ Int. 49 (2009) 783–787, https://doi.org/10.2355/ isiiinternational.49.783.
- [9] L.K. Jakobsson, M. Tangstad, T. Activities, Distributions of Calcium and Magnesium Between Silicon and CaO-MgO-SiO2 Slags at,, K (1600 °c), Metall and Materi Trans b. 46 (2015) (1873) 595–605, https://doi.org/10.1007/s11663-014-0268-8.
- [10] M.D. Johnston, M. Barati, Distribution of impurity elements in slag-silicon equilibria for oxidative refining of metallurgical silicon for solar cell applications, Sol. Energy. Mater. Sol. Cells. 94 (2010) 2085–2090, https://doi.org/10.1016/j. solmat.2010.06.025.
- [11] J. Safarian, G. Tranell, M. Tangstad, Boron removal from silicon by CaO-Na2O-SiO2 Ternary slag, Metallurgical and Materials Transactions e. 2 (2015) 109–118, https://doi.org/10.1007/s40553-015-0048-7.
- [12] J. Safarian, G. Tranell, M. Tangstad, Thermodynamic and kinetic behavior of B and na through the contact of B-doped silicon with Na2O-SiO2 slags, Metall and Materi Trans b. 44 (2013) 571–583, https://doi.org/10.1007/s11663-013-9823-y.
- [13] M. Fang, C. Lu, L. Huang, H. Lai, J. Chen, X. Yang, J. Li, W. Ma, P. Xing, X. Luo, Multiple slag operation on boron removal from metallurgical-grade silicon using Na₂O-SiO₂ slags, Ind. Eng. Chem. Res. 53 (2014) 12054–12062, https://doi.org/ 10.1011/join/04/27c.
- [14] J. Wu, W. Ma, B. Jia, B. Yang, D. Liu, Y. Dai, Boron removal from metallurgical grade silicon using a CaO–Li2O–SiO2 molten slag refining technique, J. Non-Crystalline Solid. 358 (2012) 3079–3083, https://doi.org/10.1016/j. jnoncrysol.2012.09.004.
- [15] H. Lai, L. Huang, C. Lu, M. Fang, W. Ma, P. Xing, J. Li, X. Luo, Reaction mechanism and kinetics of boron removal from metallurgical-grade silicon based on Li2O-SiO2 slags, JOM 68 (2015) (1989) 2371–2380, https://doi.org/10.1007/s11837-015-1656-5
- [16] J. Wu, F. Wang, W. Ma, Y. Lei, B. Yang, Thermodynamics and kinetics of boron removal from metallurgical grade silicon by addition of high basic potassium Carbonate to calcium silicate slag, Metall and Materi Trans b. 47 (2016) 1796–1803, https://doi.org/10.1007/s11663-016-0615-z.
- [17] Y. Li, J. Wu, W. Ma, B. Yang, Boron removal from metallurgical grade silicon using a refining technique of calcium silicate molten slag containing potassium Carbonate, SILICON 7 (2014) 247–252, https://doi.org/10.1007/s12633-014-9222-2.
- [18] L. Huang, J. Chen, M. Fang, S. Thomas, A. Danaei, X. Luo, M. Barati, Clean enhancing elimination of boron from silicon kerf using Na2O-SiO2 slag treatment, J. Clean. Prod. 186 (2018) 718–725, https://doi.org/10.1016/j. iclepro.2018.03.152.
- [19] D. Wang, Z. Wang, Z. Wang, G. Qian, X. Gong, L. Xin, Silicon recovery from silicon sawing waste by removal of SiC impurity via CaO-SiO2-Na2O slag absorption, Sep. Purif. Technol. 231 (2020) 115902, https://doi.org/10.1016/j. seppur 2019 115002
- [20] G.X. Wang, B. Pei, J.D. Litster, High temperature behavior of Si3N4-bonded SiC bricks in blast furnace environment, ISIJ Int. 38 (1998) 1326–1331, https://doi.org/10.2355/isijinternational.38.1326.

- [21] J. Du, A.N. Cormack, The medium range structure of sodium silicate glasses: a molecular dynamics simulation, J. Non-Crystalline Solid. 349 (2004) 66–79, https://doi.org/10.1016/j.jnoncrysol.2004.08.264.
- [22] C.W. Bale, E. Bélisle, P. Chartrand, S.A. Decterov, G. Eriksson, K. Hack, I.-H. Jung, Y.-B. Kang, J. Melançon, A.D. Pelton, C. Robelin, S. Petersen, FactSage thermochemical software and databases recent developments, Calphad 33 (2009) 295–311, https://doi.org/10.1016/j.calphad.2008.09.009.
- [23] P. Nikolopoulos, S. Agatho Pou Los, G.N. Angelopoulos, A. Naoumidis, H. Grübmeier., Wettability and interfacial energies in SiC-liquid metal systems, J Mater Sci. 27 (1992) 139–145, https://doi.org/10.1007/bf02403656.
- [24] C. Le Losq, D.R. Neuville, W. Chen, P. Florian, D. Massiot, Z. Zhou, G.N. Greaves, Percolation channels: a universal idea to describe the atomic structure and dynamics of glasses and melts, Sci Rep. 7 (2017), https://doi.org/10.1038/s41598-017-16741-3.
- [25] M. Micoulaut, M. Bauchy, Topology and rigidity of silicate melts and glasses, Rev. Mineral. Geochem. 87 (2022) 163–191, https://doi.org/10.2138/rmg.2022.87.04.
- [26] J. Lee, S.K. Lee, Probing the homogeneous distribution of sodium atoms in silicate glasses, Acta Mater. 241 (2022) 118413, https://doi.org/10.1016/j. actamat.2022.118413.
- [27] M. Chen, B. Zhao, Viscosity measurements of the SiO2–K2O–CaO system relevant to biomass slags, Fuel 180 (2016) 638–644, https://doi.org/10.1016/j. firel_2016_04_009
- [28] L.K. Jakobsson, M. Tangstad, Distribution of boron between silicon and CaO-MgO-Al2O3-SiO2 slags, Metall and Materi Trans b. 45 (2014) 1644–1655, https://doi.org/10.1007/s11663-014-0088-x.
- [29] G. Wu, E. Yazhenskikh, K. Hack, E. Wosch, M. Müller, Viscosity model for oxide melts relevant to fuel slags. Part 1: pure oxides and binary systems in the system SiO2–Al2O3–CaO–MgO–Na2O–K2O, Fuel Process. Technol. 137 (2015) 93–103, https://doi.org/10.1016/j.fuproc.2015.03.025.
- [30] G. Wu, E. Yazhenskikh, K. Hack, M. Müller, Viscosity model for oxide melts relevant to fuel slags. Part 2: The system SiO 2 –Al 2 O 3 –CaO–MgO–Na 2 O–K 2 O, Fuel Process. Technol. 138 (2015) 520–533. https://doi.org/10.1016/j. fuproc.2015.06.031.
- [31] G. Qian, Y. Sun, D. Wang, Z. Wu, Z. Wang, W. Ma, Design of Refining Slag Based on structural modifications associated with the boron removal for SoG-si, Materials. 15 (2022) 3107. https://doi.org/10.3390/ma15093107.
- [32] M. Zhu, G. Wu, A. Azarov, E. Monakhov, K. Tang, M. Müller, J. Safarian, Effects of La2O3 addition into CaO-SiO2 slag: structural evolution and impurity Separation from si-sn alloy, Metall Mater Trans b. 52 (2021) 3045–3063, https://doi.org/ 10.1007/s11663-021-02232-4.
- [33] C. O'Shaughnessy, G.S. Henderson, H.W. Nesbitt, G.M. Bancroft, D.R. Neuville, The influence of modifier cations on the raman stretching modes of Q n species in alkali silicate glasses, J Am Ceram Soc. 103 (2020) 3991–4001, https://doi.org/10.1111/ jace.17081.
- [34] L. Cormier, D.R. Neuville, Ca and na environments in Na2O-CaO-Al2O3-SiO2 glasses: influence of cation mixing and cation-network interactions, Chem. Geol. 213 (2004) 103–113, https://doi.org/10.1016/j.chemgeo.2004.08.049.
- [35] M.D. Johnston, M. Barati, Effect of slag basicity and oxygen potential on the distribution of boron and phosphorus between slag and silicon, J. Non-Crystalline Solid. 357 (2011) 970–975, https://doi.org/10.1016/j.jnoncrysol.2010.10.033.
- [36] K. Suzuki, N. Sano, Thermodynamics for removal of boron from metallurgical silicon by flux treatment, 10th European Photovoltaic Solar Energy Conference (1991) 273–275, https://doi.org/10.1007/978-94-011-3622-8_68.
- [37] J.F. White, C. Allertz, S. Du, The thermodynamics of boron extraction from liquid silicon using SiO2–CaO–MgO slag treatment, IJMR. 104 (2013) 229–234, https:// doi.org/10.3139/146.110867.
- [38] J. Safarian, M. Tangstad, Wettability of silicon Carbide by CaO-SiO2 slags, Metall Mater Trans b. 40 (2009) 920–928, https://doi.org/10.1007/s11663-009-9292-5.
- [39] D. Leenov, A. Kolin, Theory of Electromagnetophoresis. I. Magnetohydrodynamic forces Experienced by spherical and symmetrically oriented cylindrical Particles, J. Chem. Phys. 22 (1954) 683–688, https://doi.org/10.1063/1.1740149.
- [40] L. Espié, B. Drevet, N. Eustathopoulos, Experimental study of the influence of interfacial energies and reactivity on wetting in metal/oxide systems, Metall Mater Trans a. 25 (1994) 599–605, https://doi.org/10.1007/bf02651601.
- [41] Y. Li, Z. Li, L. Zhang, X. Wen, C. Ren, Y. Yu, Silicon recovery from si sawing waste through slag refining, Sep. Purif. Technol. 274 (2021) 119065, https://doi.org/ 10.1016/j.seppur.2021.119065.
- [42] M. Kadkhodabeigi, J. Safarian, H. Tveit, M. Tangstad, S.T. Johansen, Removal of SiC particles from solar grade silicon melts by imposition of high frequency magnetic field, Trans. Nonferrous Met. Soc. China. 22 (2012) 2813–2821, https:// doi.org/10.1016/s1003-6326(11)61537-9.
- [43] Y. Li, D. Pan, L. Zhang, H. Duan, X. Lei, W. Chen, J. Li, Characterization of SiC and Si3N4 inclusions in solar cell si scraps and their motion at the Si/slag interface, J. Mater. Res. Technol. 17 (2022) 2220–2228, https://doi.org/10.1016/j. jmrt.2022.01.157.